

**Non-equilibrium plasma-assisted dry reforming of methane over shape-controlled CeO₂ supported ruthenium catalysts**

Journal:	<i>Journal of Materials Chemistry A</i>
Manuscript ID	TA-ART-02-2023-001196.R1
Article Type:	Paper
Date Submitted by the Author:	21-Apr-2023
Complete List of Authors:	Ahasan, Md Robayet; The University of Alabama, Metallurgical and Materials Engineering Hossain, Monir; The University of Alabama, Metallurgical and Materials Engineering Ding, Xiang; Peking University Wang, Ruigang; The University of Alabama, Metallurgical and Materials Engineering

Non-equilibrium plasma-assisted dry reforming of methane over shape-controlled CeO₂ supported ruthenium catalysts

Md Robayet Ahasan,¹ Md Monir Hossain,¹ Xiang Ding,² and Ruigang Wang^{1*}

*Email: rwang@eng.ua.edu

¹Department of Metallurgical and Materials Engineering, The University of Alabama, Tuscaloosa, AL 35487, United States

²College of Urban and Environmental Sciences, Peking University, Beijing 100871, China

Abstract:

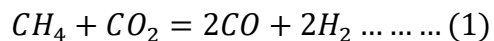
In this report, CeO₂ and SiO₂ supported 1 wt% Ru catalysts were synthesized and studied for dry reforming of methane (DRM) by introducing non-thermal plasma (NTP) in a dielectric barrier discharge (DBD) fixed bed reactor. From quadrupole mass spectrometer (QMS) data, it is found that introducing non-thermal plasma in thermo-catalytic DRM promotes higher CH₄ and CO₂ conversion and syngas (CO+H₂) yield than those under thermal catalysis only conditions. According to H₂-TPR, CO₂-TPD, and CO-TPD profiles, reducible CeO₂ supported Ru catalysts presented better activity compared to irreducible SiO₂ supported Ru counterparts. For instance, the molar concentration of CO and H₂ were 16% and 9%, respectively, for plasma-assisted thermo-catalytic DRM at 350 °C, while no apparent conversion was observed at the same temperature for thermo-catalytic DRM. Highly energetic electrons, ions, and radicals under non-equilibrium and non-thermal plasma conditions are considered to contribute to the activation of strong C-H bond in CH₄ and C-O bond in CO₂, which significantly improves the CH₄/CO₂ conversion during DRM reaction at low temperatures. At 450 °C, the 1 wt% Ru/CeO₂ nanorods sample showed the highest catalytic activity with 51% CH₄ and 37% CO₂ conversion compared to 1 wt% Ru/CeO₂ nanocubes

(40% CH₄ and 30% CO₂). These results clearly indicate that support shape and reducibility effect for the plasma-assisted DRM reaction. This enhanced DRM activity is ascribed to the surface chemistry, and defect structures of CeO₂ nanorods support that can provide active surface facets, higher amounts of mobile oxygen and oxygen vacancy, and other surface defects.

Keywords: Non-thermal plasma; non-equilibrium conditions; dry reforming of methane; ruthenium; CeO₂ support.

1. Introduction:

The production of syngas (mixture of H₂ and CO) for Fischer-Tropsch synthesis (F-T synthesis) using dry reforming of methane (DRM, **Equ. 1**) represents a growing strategical interest to simultaneously reduce two major greenhouse gases (GHG, mainly CO₂ and CH₄) emission aiming at limiting global climate change. In fact, the depletion of conventional oil reserves and its environmental consequences have received considerable critical attention to pursuing an alternative roadmap for the global energy demand outlook [1]. Among various potential solutions, simultaneous conversion and reuse of two primary GHG (CO₂ and CH₄) via catalytic DRM reaction into fuels and value-added chemicals have been considered as one of the attractive strategies [2]. However, due to the sp³ hybridization, the high C-H bond dissociation energy (434 kJ/mol) in CH₄ and C=O bond dissociation energy (532 kJ/mol) in CO₂ require relatively high temperatures to overcome the thermodynamic energy barriers in heterogeneous gas-solid thermal catalysis, which can result in catalyst sintering deactivation and coking formation. For example, thermally catalytic DRM and its syngas production, given in **Equ. 1**, can only be achieved with relatively high temperatures (627–1000 °C) [3,4].



Over several lab scale single step conversion methods of CO₂ & CH₄ such as thermo-chemical [5], electrochemical [6], or photochemical methods, recently non-thermal plasma reactor has emerged as a powerful platform for DRM conversion. For example, Andersen et al. reported that at ambient pressure and temperature, a CO₂ and CH₄ conversion of ~22% and ~33% was achieved, respectively, by introducing non-equilibrium plasma for DRM reaction, while a series of Al₂O₃ supported catalysts can be added to tune the selectivity to H₂ and CO, H₂/CO molar ratio, and selectivity to different hydrocarbons and oxygenates [7–9].

For plasma-assisted catalytic conversion via DRM, various radicals, ions, electrons, and excited intermediate species can be generated by high-energy electrons and ionized gases once the breakdown voltage to form a plasma discharge is reached. Thus, high temperature and pressurized conditions in the thermal catalytic reactor are replaced by highly energetic electrons and abundant radicals/ions in plasma-assisted catalytic reactors. These excited species, typically not available in thermal reactors, present a great advantage of plasma-assisted catalytic reactions that can operate in relatively mild conditions. For example, the chemical reactions in dielectric barrier discharge (DBD) reactors, especially at low temperatures, are mainly governed by electron temperature rather than reactor gas temperature, which controls the bond activation/dissociation and recombination processes of gas molecules. Several experimental and computational research has suggested that the synergic effect of the combination between the plasma and the catalysts can significantly enhance the gas conversion and product selectivity in DRM [10–12]. Many catalysts have been tested over the last few decades for DRM via thermal catalysis, usually operated in the 650-1000 °C temperature range. Noble metals (Rh and Ru) are well known for their high catalytic activities in DRM, but nickel-based catalysts are widely used due to their lower cost but have coke

formation issues [13]. For plasma-assisted catalytic DRM, Ru over TiO₂ [14], Al₂O₃ [15], and MgO [16] has been demonstrated that plasma has a profound effect on their catalytic activity. In addition, the kinetic studies showed that coordinately unsaturated Ru surface atoms were more active than those in low-index crystal planes, predominately exposed on large crystallites. Meanwhile, some literature reported the stabilization of Ru species over CeO₂ support by mild oxidative pretreatment [17,18].

In the supported catalysts, the role of catalyst support mainly acts to provide a high surface area to disperse catalytically active metal or metal oxide clusters for better distribution and thermal stability [19,20]. Among various catalyst supports, CeO₂ has been widely investigated because of its enriched mobile surface oxygen, surface oxygen vacancy, and other surface defects, which are attributed to facilitating the catalyst-CeO₂ interaction and gas adsorption (i.e., CO₂ adsorption) due to the reversible reaction between Ce⁴⁺ and Ce³⁺. The facile redox Ce⁴⁺/Ce³⁺ transition in CeO_{2-x} has led to a proliferation of many fundamental catalyst-support interaction studies. The concentration of Ce³⁺ is generally proportional to oxygen vacancy concentration, which illustrates the effectiveness of oxygen exchange between the catalyst and CeO₂ support [21]. In addition, the occupied 4f-orbital electrons of Ce³⁺ ions can promote the electronic interaction between reducible CeO₂ and metal nanoparticles [22]. To further improve the oxygen exchange capability of CeO₂, it was discovered that specific shapes of CeO₂ nanoparticles allow a controlled supply of oxygen in a redox-related catalytic reaction such as octahedra, rods, cubes, and spheres [23–25]. For example, the exposed surfaces of CeO₂ nanocubes (CeO₂-NC) with {1 0 0}, CeO₂ nanorods (CeO₂-NR) with {110} and {100} or {1 1 1} and CeO₂ nanooctahedra (CeO₂-NO) with {1 1 1} facets have been most studied for catalytic applications [8, 26–28]. Thanks to this unique oxygen storage capacity (OSC) property, reducible CeO₂-based oxides have been utilized in versatile catalytic reactions.

On the other side, irreducible SiO_2 with a high surface area has also been frequently used as oxide catalyst support, mainly aiming at enhancing the metal cluster dispersion and thermal stability. In general, SiO_2 is considered inert catalyst support in nature due to the high oxygen vacancy formation energy and low isoelectric point (IEP) of SiO_2 (IEP ~ 2), and it forms weak or no interaction with metal catalyst clusters [29].

In this work, we report 1 wt% Ru supported on irreducible SiO_2 and reducible CeO_2 with two different morphologies (CeO_2 -NR and CeO_2 -NC), exposing facets with $\{110\}$ / $\{100\}$ / $\{111\}$ and $\{100\}$ respectively to investigate the non-thermal plasma influence as well as the support shape effect on the DRM reaction under non-equilibrium conditions.

2. Experimental section

2.1. Catalyst preparation

2.1.1. Preparation of catalyst supports

SiO_2 support was synthesized by a modified Stober method from our previous research [30,31]. First, 158 mL absolute ethanol, 7.8 mL NH_4OH (28% NH_3 in H_2O), and 2.8 mL deionized water were introduced in a 250 mL round-bottom flask. The flask was heated to 50 °C under vigorous stirring. Then, 5.8 mL (TEOS 99%) was added dropwise to the solution under vigorous magnetic stirring, and this stirring continued for another 24 h at 50 °C to get complete hydrolysis. The sample was obtained by drying the suspension at 70 °C for 24 h.

CeO_2 nanorods (NR) and CeO_2 nanocubes (NC) were synthesized using a hydrothermal method, according to our previous research methodology [32–34]. For CeO_2 NR, firstly, 8 mL of 6.0 M NaOH (VWR, 99%) solution was added dropwise to 88 mL of 0.1 M $\text{Ce}(\text{NO}_3)_3 \cdot 6\text{H}_2\text{O}$ (Acros

Organics, 99.5%) solution and appropriately mixed in a 200 mL liner. The mixture was stirred approximately for about 15 s, and the lid of the Teflon liner was closed. The Teflon liner was then put into a stainless-steel autoclave and sealed tightly. The stainless-steel autoclave was heated to 90 °C and kept at this temperature for 48 h. After the hydrothermal reaction, the precipitate materials were washed thoroughly with 500 mL deionized water to remove any residual ions (Na^+ , NO_3^-), then washed with 50 mL ethanol to avoid hard agglomeration of the nanoparticles and dried in air at 60 °C for 12 h. The dried sample was collected and ground gently with mortar and pestle. The preparation of CeO_2 NC followed the same procedure; however, the autoclave was kept at 150 °C instead of 90 °C for 48 h.

2.1.2. Preparation of supported catalysts

1.0 wt% Ru was loaded onto CeO_2 NR, CeO_2 NC and SiO_2 by impregnating the support powders with an aqueous solution of $\text{Ru}(\text{NO})(\text{NO}_3)_3$. Specifically, individual 0.99 g of CeO_2 NR, CeO_2 NC, and SiO_2 powder was put into 100 mL deionized water separately in three 200 mL beakers. $\text{Ru}(\text{NO})(\text{NO}_3)_3$ (Alfa Aesar) equivalent to 1 wt% Ru was dissolved in each suspension solution of the support powders. The suspension solutions were mixed properly using magnetic stirring followed by dropwise addition of 0.5 M aqueous solution of ammonium hydroxide ($\text{NH}_3 \cdot \text{H}_2\text{O}$, BDH, 28-30 vol%) to tune the pH value of the suspension to ~ 9 . Then the precipitates were initially heated at 80 °C under stirring (400 rpm) for 4 h. Finally, the precipitates were continuously heated at 100 °C to evaporate water and transferred into a drying oven kept overnight. To obtain fine powder, mortar and pestle were used for grinding and left in an air furnace for calcination at a rate of 10 °C/min up to 350 °C and maintained at this temperature for 5 h. These samples were labeled as 1.0 wt% Ru/ CeO_2 NP-o (o refers to the oxidized sample, and NP represents NR or NC) and

1.0 wt% Ru/SiO₂-o. Finally, some of the powder samples were further reduced by heating up in a 5% H₂/Ar flow (200 mL min⁻¹) at a rate of 10 °C/min up to 300 °C and maintained at this temperature for 5 h. After cooling down to room temperature under H₂ atmosphere, these samples were labeled as 1.0 wt% Ru/CeO₂ NP-r (r refers to the reduced sample) and 1.0 wt% Ru/SiO₂-r.

2.2. Catalyst characterization

Powder X-ray diffraction (XRD) characterization was conducted on a Phillips X'Pert MPD diffractometer with a copper K α radiation source ($\lambda=0.154$ nm) at 40 kV and 40 mA. The samples were scanned with a scan rate of 0.5° min⁻¹ from 2θ range between 10° and 90°. JADE software was used to determine each catalyst sample's lattice parameters and average crystallite size based on the recorded XRD patterns.

At 77 K, the BET surface area was determined using single-point nitrogen physisorption. A Micromeritics AutoChem II 2920 chemisorption analyzer was used to characterize H₂-temperature programmed reduction (H₂-TPR). The powder samples (85-95 mg) were placed in a quartz U-tube sandwiched between two pieces of quartz wool, then heated at a rate of 10 °C/min from 30 °C to 900 °C. During the H₂-TPR, the samples were reduced at a flow rate of 50 mL/min in a 10 vol.% H₂-90 vol.% Ar gas mixture. A thermal conductivity detector (TCD) was used to monitor the quantity of H₂ uptake during the reduction, which was calibrated using a quantitative reduction of CuO to metallic copper.

Carbon dioxide temperature-programmed desorption (CO₂-TPD) was performed using the same Micromeritics AutoChem II 2920 instrument as H₂-TPR to investigate the interaction of CO₂ with the catalyst/support surface. First, the quartz wool sandwiched powder sample was put into a quartz U-tube microreactor and heated from room temperature to 400 °C with He stream (flowrate:

50 mL/min) to remove residual moisture. After cooling to room temperature, 10 vol.% CO₂ - 90 vol.% He mixture gas was supplied with a flowrate at 50 mL/min through the sample for 60 min. The sample was then heated up to 900 °C at a linear ramping rate of 10 °C/min under helium gas. A thermal conductivity detector was used to evaluate the desorption behavior of CO₂ at elevated temperatures.

High-resolution transmission electron microscopy (HRTEM) images were obtained by using an FEI Tecnai F20 with an acceleration voltage of 200 kV while JEOL 7000 FE SEM was used to obtain energy dispersive X-ray spectroscopy data (EDAX system). For the TEM sample preparation, the sample went through ultrasonic dispersion of the powder in ethanol. One or two drops of the suspension solution were deposited on ultrathin carbon film supported by a 400-mesh copper grid (Ted Pella Inc.) and then dried for 2 h before analysis.

Kratos Axis Ultra DLD spectrometer using monochromatic Al K α ($h\nu = 1486.6$ eV) source under ultra-high vacuum (10^{-10} Torr) was used to acquire X-ray photoelectron spectroscopy (XPS) data, and carbon (C) 1s at 284.8 eV was used for calibration of binding energies (BE). The fitting and deconvolution of the spectra were conducted using the CASA XPS software.

Non-destructive Raman characterization of the catalysts was done by Horiba LabRAM HR 800 Raman spectrometer (equipped with a 100 long working distance objective, NA = 0.60) in the spectral window from 100 to 1200 cm⁻¹. A diode-pumped solid-state (DPSS) laser system (Laser Quantum MPC6000) tuned at $\lambda = 532$ nm was used for excitation. Prior to each analysis, the spectrometer was calibrated using a single crystal Si wafer.

2.3. Catalytic activity measurements

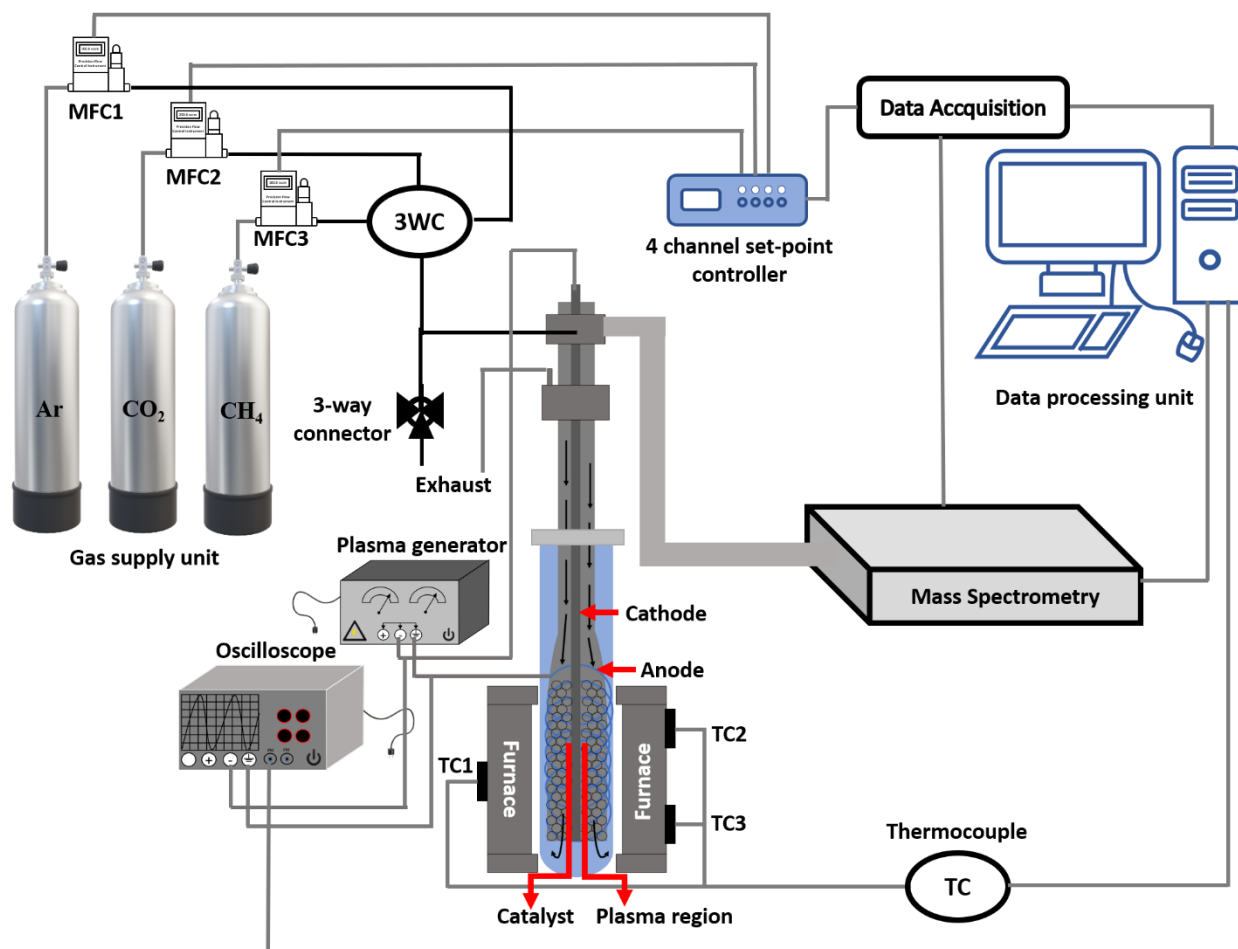


Fig. 1 Schematic of reactor setup for plasma-assisted DRM test station. The red color arrow sign identified the plasma and catalyst region, including the anode and cathode. TC1, TC2, TC3 - Thermocouples, 3WC- three-way gas flow controller, and MFC-1, MFC-2, MFC-3 - mass flow controllers.

The components of the DBD reactor can be divided into four parts: a gas delivery system, a central quartz reactor tube, an experimental control section, and a flow gas analysis system. **Fig. 1** illustrates the schematic diagram of the whole plasma reactor system. The gas supply system includes three Brooks GF040 Multiflo thermal mass flow controllers (MFC) with <1 s response

time, represented by MFC-1, MFC-2, and MFC-3. The flow of Ar, CH₄, and CO₂ with purity >99.99% from Airgas was controlled by these MFCs. A computer interface with a NI card loaded with a home-written MATLAB GUI code was used to control the gas flow of MFCs. Each complete operation of the plasma-assisted DRM reaction consists of a 7 min reduction cycle followed by a 6 min purge with pure Ar gas. During the reduction, the gas mixture of CH₄ and CO₂ flowed with a total flowrate of 350 sccm (CH₄ : CO₂ = 100 : 250 sccm), while in the purging step, 100% Ar was flowed to purge the reactor for the subsequent reduction cycle.

For plasma generation, the main reactor includes two concentric quartz tubes placed inside an ATS 3210 split tube furnace that can heat the reactor to 1100 °C and provide an isothermal environment. Three thermocouples TC1, TC2, and TC3 are used to measure the furnace temperature during plasma and thermal DRM reactions. The 2" length inner quartz tube has an outer diameter (OD) of ¼" with an expansion section of 3/8" inner diameter (ID). This tube links with the supply gas system so that reactive gases flow into the inner tube first. The other side of the inner quartz tube with an open end was placed inside the outer quartz reactor tube. The outer quartz tube is 1" OD and closed at the bottom end. The catalyst sample was dispersed in quartz wool and placed inside the expansion section of the inner quartz tube where the plasma was generated. After entering the inner tube, the reactant gases interact with catalysts and plasma and go through the open end of that tube. The closed outer tube reverses the direction of the gases and flows out to the exhaust. An enlarged schematic of the plasma-catalysis reactor area was shown in **Fig. S1**.

The exhaust gas system is analyzed using a quadrupole mass spectrometer (QMS, model: MAX300-EGA from Extrel, 300 ms, 1-250 amu detectability) and a customized tunable diode quantum cascade laser absorption spectroscopy (TDLAS) system. The QMS is connected with a tiny capillary quartz probe (0.80 mm OD, 0.53 mm ID) to sample the gases and measure time-

resolved species at the probe end location, at the exit of the inlet tube expansion section where the catalyst is placed in plasma. But the TDLAS system is connected at the exhaust line for detecting C-2 based species such as C_2H_2 , C_2H_4 , and C_2H_6 . Before the operation, QMS is calibrated by flowing a known mixture of gases. All gases (CO_2 , CO , H_2 , CH_4 , Ar , O_2) flowed simultaneously for calibration. Typically, increasing the gas flow rate decreases the gas residence time in the reaction region, while the QMS sensitivity to species measurements also decreases due to the large dilution of H_2 by the balance gas Ar [35,36]. Thus, a lower flow rate increases gas residence time and makes it comparable to reaction time constants (5–10 s), and therefore we choose an optimum total volume flow rate of 350 sccm for our experiments. According to a calculation by dividing the reaction region volume by the gas volume flow rate at the reactor temperature, the gas residence time at the catalyst and plasma region is <0.5 s. The expanded part of the inner quartz reactor tube contains two coaxial electrodes. One electrode is placed at the center of the inner inlet tube inside a 0.063 ID ceramic tube as a dielectric barrier. Another is placed on the outside of the expansion section spirally surrounding the tube, giving rise to Dielectric Barrier Discharge (DBD) which produces non-equilibrium plasma. Those two electrodes are connected to a plasma driver (PVM500-2500 from Amazing1.com) integrated with a voltage regulator (1-40 kV) with a 20-70 kHz discharge frequency to generate the plasma.

In our experiment, the total flow rate of gases mixture was maintained at 350 sccm (standard cubic centimeter/min) during the reduction step. The mixture of gases contains CH_4 (100 sccm or 28.6 vol.%) and CO_2 (250 sccm or 71.4 vol.%).

According to the previous reports [37-38], it was claimed that the metastable O species could accelerate the dissociation of CH_4 and promote the CH_4 conversion. In this project, in the supplied gases of DRM reaction, CO_2 is the only source of oxygen. To reduce the CH_x recombination and

the formation of byproducts, excess amount of CO₂ supply was used in this project (CH₄: 100 sccm or 28.6 vol.% and CO₂: 250 sccm or 71.4 vol.%). The average gas velocity is ~6.48 cm/s at 25 °C in the reactor environment. The measured plasma power was 10.2 to 13.6 W during the reduction cycle (DRM reaction). This variation possibly happened due to gas breakdown voltage and concentration [38]. Similarly, Yabe et al. [39] also reported this power variation for different Ni/M-ZrO₂ catalysts. It should be noted that a portion of plasma power is lost by heating the cable, electrodes, and reactor wall from the applied plasma power. For instance, Nozaki et al. [40] reported a maximum of 25% power consumption for increasing gas temperature theoretically, while it was 15% in practical experiments. Only Ar was supplied during the purging step at a flowrate of 350 sccm. All experiments were conducted at 1 atm pressure and in the temperature range of 150–450 °C. A single periodic operation consists of 6 min purge and a 7 min reduction step.

2.4. Performance parameters

The conversion rate is defined as the molar ratio of how much the reactant is converted according to the input. The yield of a reaction is calculated by the ratio of the desired product formed (in moles) to the total amount that could have been made (if the yield of the limiting reactant is 100% and no side reaction occurs), while selectivity of a reaction is the ratio of the desired product formed (in moles) to the undesired product formed (in moles). The formula of CH₄ and CO₂ conversion and product (H₂ and CO) selectivity and yield of a DRM reaction are given below:

$$C_{\text{CH}_4} = \frac{\text{Moles of CH}_4 \text{ Converted}}{\text{Moles of CH}_4 \text{ Input}} * 100\% \dots \dots (2)$$

$$C_{\text{CO}_2} = \frac{\text{Moles of CO}_2 \text{ Converted}}{\text{Moles of CO}_2 \text{ Input}} * 100\% \dots \dots (3)$$

$$Y_{H_2}(\%) = \frac{\text{Moles of } H_2 \text{ Produced}}{2 * \text{Moles of } CH_4 \text{ Input}} * 100\% \dots \dots (4)$$

$$Y_{CO}(\%) = \frac{\text{Moles of CO Produced}}{\text{Moles of } CH_4 \text{ Input} + \text{Moles of } CO_2 \text{ Input}} * 100\% \dots \dots (5)$$

$$S_{H_2}(\%) = \frac{\text{Moles of } H_2 \text{ Produced}}{2 * \text{Moles of } CH_4 \text{ Converted}} * 100\% \dots \dots (6)$$

$$S_{CO}(\%) = \frac{\text{Moles of CO Produced}}{\text{Moles of } CH_4 \text{ Converted} + \text{Moles of } CO_2 \text{ Converted}} * 100\% \dots \dots (7)$$

3. Results and discussion:

3.1 Powder X-ray diffraction and TEM/EDX analysis

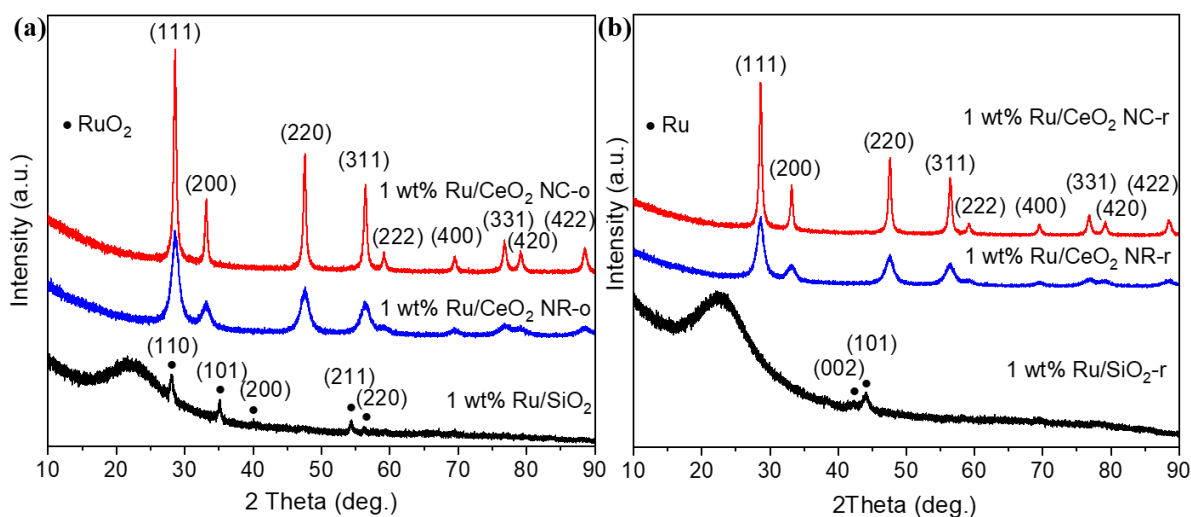


Fig. 2 XRD patterns of 1 wt% Ru/SiO₂, 1 wt% Ru/CeO₂ NR, 1 wt% Ru/CeO₂ NC for (a) oxidized and (b) reduced samples.

Fig. 2 shows the XRD patterns of CeO₂ and amorphous SiO₂ supported 1 wt% Ru catalysts after the oxidation (**Fig. 2a**) and reduction (**Fig. 2b**) treatments. The XRD patterns of CeO₂ NR and NC match well with the face-centered cubic fluorite structure of ceria (JCPDS # 34-0394 and space group Fm3m). The XRD pattern of SiO₂ “aligns” with the standard JCPDS card of amorphous

SiO₂ (PDF#00-038-0360). Three intense diffraction peaks appeared at 2θ of 28.6, 47.5, and 56.4, corresponding to the crystal planes of CeO₂ (111), (220), and (311), which confirmed that CeO₂ NR and NC with impregnated RuO_x maintained their fluorite-type structures, followed by calcination at 350 °C for 5 h in air and H₂ reduction treatment at 300 °C for 5 h [41]. The diffraction peaks for CeO₂ NR and CeO₂ NC are in similar positions. However, their relative intensities and sharpness indicate that CeO₂ NR has a smaller crystalline size and/or smaller crystalline domains compared to those of CeO₂ NC. For both oxidized and reduced 1 wt% Ru/CeO₂ NR and NC, no apparent diffraction peaks were detected for either RuO or Ru. Possible explanations for the absence of RuO_x (0 ≤ x ≤ 1) species are a) RuO_x diffusion into CeO₂ lattice or formation of Ru-O-Ce solid solution, b) highly dispersed RuO_x on CeO₂ and c) small RuO_x loading (1 wt%) [42]. Meanwhile, the XPS and *in situ* DRIFTS data revealed the presence of RuO_x species on both CeO₂ NR and NC.

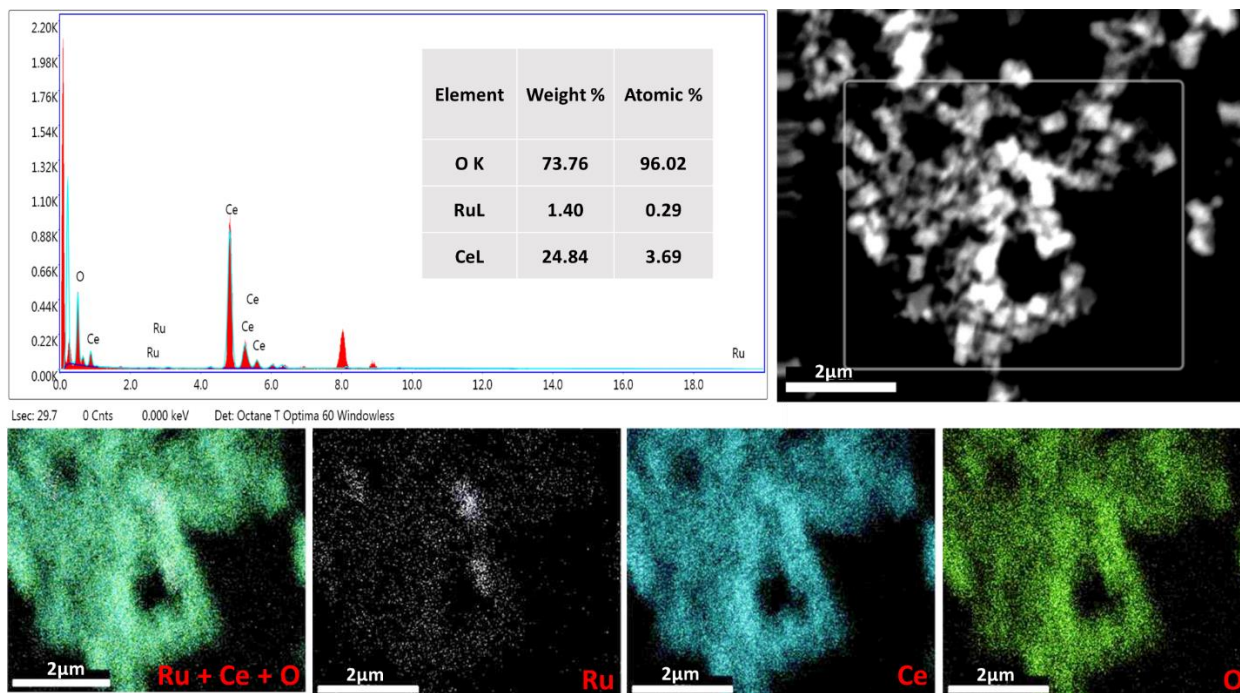


Fig. 3 EDS line spectrum and elemental mapping of 1 wt% Ru/CeO₂ NC-r catalyst.

The estimated crystalline sizes of SiO₂ and CeO₂ supported RuO_x samples are enlisted in Table 1 using the Scherrer equation from XRD peak analysis. Besides, the EDS line spectrum and elemental mapping are also presented in **Fig. 3**, suggesting a uniform distribution of RuO_x over CeO₂. On the other hand, after calcination and reduction treatment of 1 wt% Ru/SiO₂, as shown in **Fig. 2**, the XRD profiles show the peaks of RuO₂ for the calcined sample and metallic Ru for the reduced sample. Major RuO₂ peaks are observed at $2\theta = 28.2, 35.3, \text{ and } 54.6$, while metallic Ru peaks at $42.3 \text{ and } 44$ with relatively low peak intensity.

3.2 H₂-temperature programmed reduction (H₂-TPR)

The H₂-TPR profiles of the prepared catalysts can be utilized to investigate oxygen release capacity or H₂ consumption and identify possible surface metal/oxide species and the nature of active sites. As shown in **Fig. 4**, the H₂-TPR signals show a few hydrogen consumption peaks corresponding to the reduction of surface oxygen (O_s) and bulk oxygen (O_b) [33]. All of the oxidized and reduced CeO₂ samples display three reduction major peaks: less than 200 °C, 200 °C-500 °C and greater than 500 °C [43]. In the region below 200 °C, 1 wt% Ru/CeO₂ NR-o presents two reduction peaks at 105 °C and 129 °C resulting from multiple oxidation states of RuO_x due to the interaction between RuO_x and CeO₂ [43]. Two similar peaks (surface oxygen reduction peaks) also appear at 115 °C and 158 °C for 1 wt% Ru/CeO₂ NC-o. Notably, the reduction peaks of 1 wt% Ru/CeO₂ NR-o appear at slightly lower temperatures than those of 1 wt% Ru/CeO₂ NC-o. The latter two regions of the oxidized CeO₂ samples have significantly lower intensity and are barely observable due to a higher amount of H₂ consumption below 200 °C and the corresponding scaling factor. After the reduction treatment of the catalysts, there is an increase in BET surface area for each catalyst. This is due to the redispersion of partially reduced RuO_x species over CeO₂ supports. For

example, Fernandez et al. [44] reported the disaggregation and transformation of large RuO_2 to small round shape Ru crystallites after reduction treatment. The H_2 -TPR profiles of the reduced sample are shown in **Fig. 4 (b)**. After the reduction treatment of two CeO_2 samples, three hydrogen consumption peaks were also observed but with a bit lower reduction temperature. For example, the O_s peak shifted from 105°C for 1 wt% Ru/CeO_2 NR-o to 82°C for 1 wt% Ru/CeO_2 NR-r while the similar peak shifted from 115°C for 1 wt% Ru/CeO_2 NC-o to 67°C for 1 wt% Ru/CeO_2 NC-r. The BET surface area, crystal size, total H_2 consumption and reduction temperature data are shown in **Table S1**. The pore size distribution and total pore volume of both 1 wt% Ru/CeO_2 NC and 1 wt% Ru/CeO_2 NR catalysts were shown in **Fig. S2**.

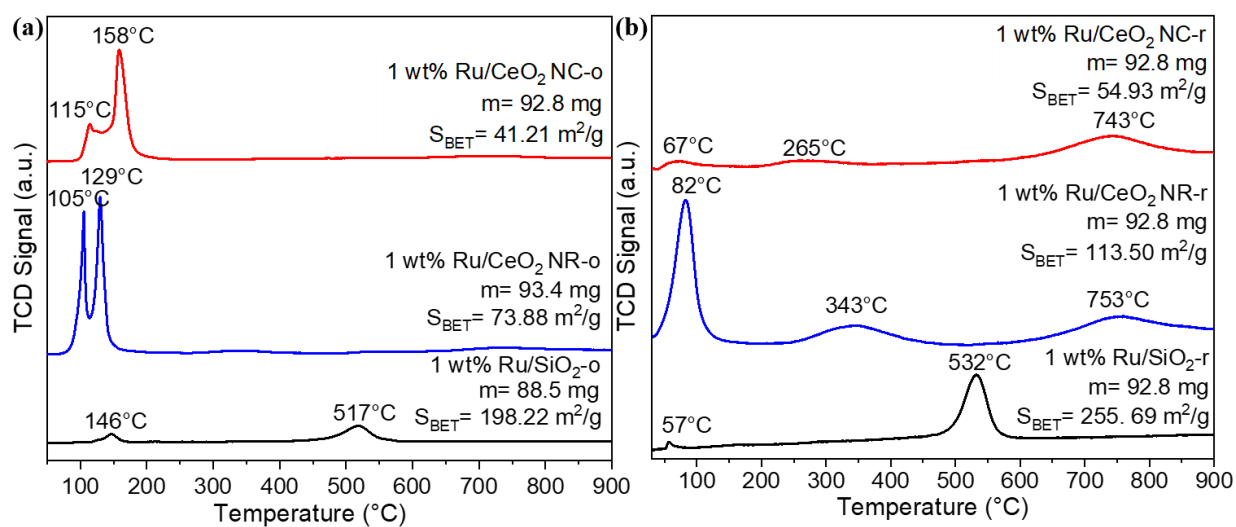


Fig. 4 H_2 -TPR profiles of CeO_2 NP and SiO_2 supported RuO_x catalysts after (a) oxidation treatment and (b) reduction treatment.

These hydrogen consumption peaks shifting after a reduction treatment are attributed to the activation of Ru catalysts [27,45]. Because after reduction treatment, metallic Ru can easily donate electrons and make the Ru-oxide support interface surrounded by electron-enriched oxygen ions

[42]. These “donated” electrons can be easily released, involve bond breakage, and promote gas conversion reactions with activated CO_2 and CH_4 species. The H_2 -TPR profile of 1 wt% Ru/ SiO_2 -o showed one low-intensity peak at 146 °C, which shifted to 57 °C for 1 wt% Ru/ SiO_2 -r. The reduction peaks at 517 °C and 532 °C for Ru/ SiO_2 present relatively low intensity compared to Ru/ CeO_2 . These reduction peaks are possibly related to 1) mixed RuO_2 - SiO_2 phases formed; 2) decomposition of precursors; 3) the reduction of RuO_2 [46,47].

3.3 CO_2 -temperature programmed desorption (CO_2 -TPD)

To better understand the CO_2 adsorption-desorption behavior and nature of different basic sites on the prepared oxidized and reduced catalysts, CO_2 -TPD measurements were carried out as the DRM reaction is initiated by an acid-base interaction, where CO_2 acts as acids towards the catalyst with base properties. Thus, the adsorption and activation of acidic CO_2 depend on the base catalyst's surface, which will determine the overall conversion and catalyst stability. The CO_2 -TPD profiles in **Fig. 5 (a-c)** demonstrate the surface basicity of SiO_2 , CeO_2 NR, and CeO_2 NC supported RuO_x , respectively. The typical CO_2 -TPD desorption profile is comprised of three fundamental group classes contribution that corresponds to weak Bronsted basic sites (e.g., surface OH groups), Lewis acid–base sites of medium strength, and low-coordination oxygen anions exhibited as strong basic sites, respectively [48]. These three classes of basic sites appeared at three temperature regions, 50-150, 150-250, and > 250 °C [49]. The CO_2 -TPD profiles of 1 wt% Ru/ SiO_2 -o and 1 wt% Ru/ SiO_2 -r consist of three desorption peaks from 300 °C to 900 °C. These three peaks appeared at 395 °C to 425 °C, 535 °C to 555 °C and 790 °C to 860 °C corresponding to CO_2 desorption from strong basic sites [50]. Thus, no weak or medium CO_2 desorption happened for Ru- SiO_2 catalysts due to poor interactions between Ru and SiO_2 .

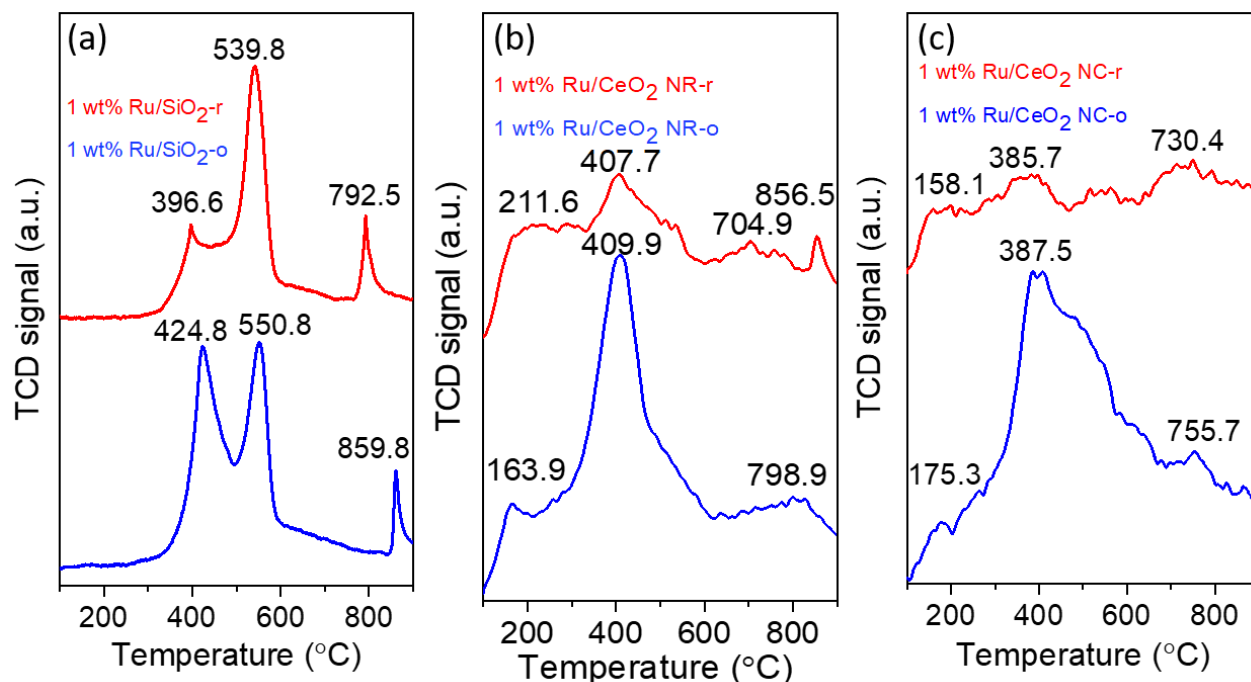


Fig. 5 CO₂-TPD profiles of the oxidized and reduced (a) SiO₂, (b) CeO₂ NR, and (c) CeO₂ NC supported RuO_x catalysts.

The desorption peaks of the reduced sample appeared at a little lower temperature than those of the oxidized catalyst due to the activation of Ru particles by the H₂ reduction treatment. The H₂ reduction treatment typically plays roles in catalyst activation including: a) the reduction of RuO_x to metallic Ru which can lead to an enhanced reaction rate of CH₄ adsorption and decomposition; b) creating oxygen vacancies due to the reduction treatment which promotes the CO₂ activation and C-O bond cleavage; c) removing the surface water/CO₂ which makes the surface more basic. The effects of the reduction treatment of CeO₂ NR and NC supported 1 wt% Ru can be clearly seen in **Fig. 5** (b, c). Both oxidized and reduced 1 wt% Ru/CeO₂ NR and 1 wt% Ru/CeO₂ NC present three CO₂ desorption peaks at 150 °C-215 °C, 380 °C-410 °C and 700 °C-850 °C, respectively. Here, the weak and moderate adsorptions at low temperature range correspond to the formation of bridged and bidentate carbonates at the 50 °C-150 °C and 150 °C-250 °C regions.

The high-temperature peaks greater than 250 °C are attributed to the formation of carboxylate and monodentate carbonates with stronger CO₂ adsorption [51]. Both of 1 wt% Ru/CeO₂ NP-o samples showed low-temperature CO₂ desorption peaks, while the reduced samples showed broader desorption peaks. This indicates that a reduced catalyst allowed a higher amount of CO₂ desorption at low temperatures, which can promote the DRM reaction. According to the literature [52], broad desorption CO₂ peaks suggest higher amount of basic sites, which can reduce the coking or deactivation of the catalyst by the reaction: $CO_2 + C = 2CO$. CO₂ adsorption on weak and moderate basic sites promotes the formation of active carbonate species on the metal-support interface of the catalysts, while CO₂ adsorption on strong basic sites could lead to direct decomposition of CH₄ and aggregation of carbon on active metal catalysts. These active carbonate species can interact with CH₄ and produce CO between the interaction of O from carbonate species and C from CH₄ decomposition. Li et al. [53] reported that CO₂ adsorption on medium-strength basic sites leads to easy activation of CO₂ than on strong basic sites. The desorption peaks of the reduced sample shifted to a lower temperature compared to oxidized 1 wt% Ru/CeO₂ NP which indicates that loading of active Ru promotes the formation of weak and medium strength basic sites and CO₂ derived species and accelerates DRM. From **Fig. 5 (b, c)**, it seems that the shape effect of CeO₂ support on CO₂ desorption is negligible from CO₂-TPD.

3.4 X-ray photoelectron spectroscopy (XPS)

In order to understand the valence states and surface chemical composition of the oxidized and reduced catalysts, XPS characterization was executed. **Fig. 6 (a-c)** shows the XPS spectra of 3d orbital of Ru and Ce and 1s orbital of O. In the case of 1 wt% Ru/CeO₂ NR-o, RuO_x is analyzed by 3d orbital of Ru, which gives intense peaks but overlapping with C 1s peaks. The deconvolution of Ru 3d core-level spectrum exhibits four different components centered at 280.61 eV, 281.81

eV, 285.21 eV, and 286.01 eV. These peaks are assigned to $\text{Ru}^{n+} 3d_{5/2}$ ($4 < n < 6$), $\text{Ru}^{6+} 3d_{5/2}$, $\text{Ru}^{n+} 3d_{3/2}$ ($4 < n < 6$) and $\text{Ru}^{6+} 3d_{3/2}$ respectively. The peaks observed at 283.71 eV and 287.81 eV could be assigned for C 1s peaks. For the reduced 1 wt% Ru/CeO₂ NR, similar four peaks are also observed with slightly lower binding energy. From these peaks, two deconvolution peaks centered at 281.31 eV and 285.61 eV still showed Ru^{n+} ($4 < n < 6$) species, while the remaining two peaks with binding energy 280.31 eV and 284.81 eV are assigned for spin-orbit coupling of $\text{Ru}^{4+} 3d_{5/2}$ and $\text{Ru}^{4+} 3d_{3/2}$ respectively [27].

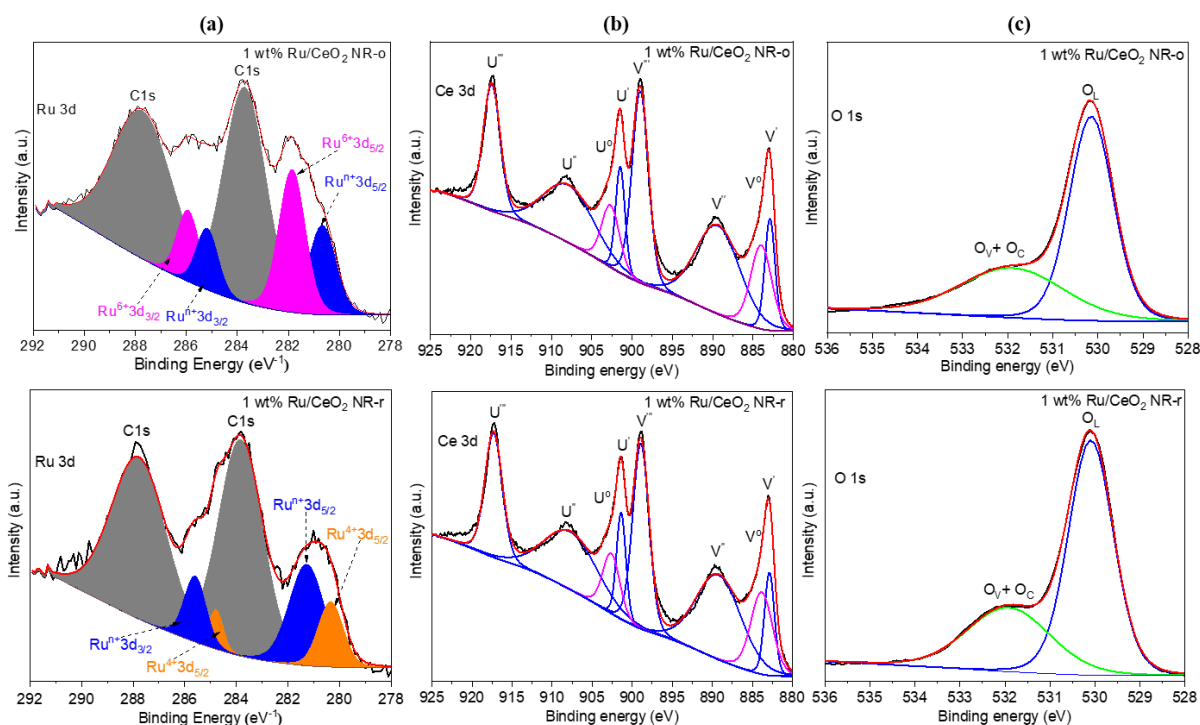


Fig. 6 XPS spectra of the 1 wt% Ru/CeO₂ NR samples after the oxidation (upper row) and reduction treatments (bottom row) for (a) Ru 3d, (b) Ce 3d, and (c) O 1s. O_v and O_c refer to the oxygen vacancy and chemisorbed oxygen, respectively.

The existence of Ru^{n+} species suggests possible electron transfer from RuO_x to CeO_{2-x} , which promotes the formation of Ru-O-Ce solid solution or increases oxygen vacancy concentration [54].

Fig. 6 (c) showed the XPS spectrum of 1s orbital of O for two CeO₂ NR samples. The broad peak of O 1s for oxidized and reduced CeO₂ NR supported RuO_x is evaluated by fitting into two components: lattice oxygen (O_L) and oxygen vacancy (O_V) as well as chemisorbed oxygen (O_C) centered at 530.11 eV and 531.91 eV, respectively. The relative content of these two oxygen species was calculated by the following formula: $O_v/(O_v + O_L)$. The relative oxygen contents are similar, with the value 50.1% and 49.5% for 1 wt% Ru/CeO₂ NR-o and 1 wt% Ru/CeO₂ NR-r, respectively. For the XPS spectra of Ce 3d shown in **Fig. 6 (b)**, there are eight peaks from four pairs of Ce 3d_{3/2} and Ce 3d_{5/2}, which correspond to Ce³⁺ and Ce⁴⁺ ions. Those peaks labeled as U° , U' , U'' and U''' belong to Ce 3d_{3/2}, and the peaks labeled as V° , V' , V'' and V''' are assigned to Ce 3d_{5/2}. The peaks located at 883.81 eV (V°) and 901.41 eV (U°) are attributed to the concentration of Ce³⁺ ions from Ce 3d_{5/2} and Ce 3d_{3/2}, respectively. The remaining peaks appeared at 882.81 eV, 889.51 eV, 898.91 eV, 901.41 eV, 908.21 eV, and 917.31 eV labeled by V' , V'' , V''' , U' , U'' and U''' represent the concentration of Ce⁴⁺ ions. The relative concentration of Ce³⁺ ions can be calculated by integrating each peak area with the equation below:

$$[Ce^{3+}] = \frac{A_{uo} + A_{vo}}{A_{uo} + A_{vo} + A_{u'} + A_{u''} + A_{u'''} + A_{v'} + A_{v''} + A_{v'''}} \dots \dots \dots (8)$$

The concentration of Ce³⁺ was 26.54% and 23.24% for the reduced and oxidized 1 wt% Ru/CeO₂ NR catalysts, respectively. One of the main reasons for a slight difference in Ce³⁺ concentrations is the reduction treatment temperature. We reduced each catalyst to 300 °C in H₂ environment. A valid reason for this low reduction treatment temperature is to maintain the shape of the CeO₂ NP because CeO₂ shape is highly influenced by temperature. As shown in **Fig. S3**, the initial reduction for CeO₂ NR started at around 350 °C. Thus, besides the small reduction of CeO₂, RuO₂ is mainly reduced by the reduction treatment and leads to an increase in oxygen vacancy concentration. From

oxidized and reduced XPS characterization data of 1 wt% Ru/CeO₂ NR, it is apparently clear that partially reduced Ruⁿ⁺ ions increase significantly along with the slight increase of Ce³⁺ ion concentration after reduction treatment. The formation of Ce³⁺ ions is believed to relate to the available oxygen vacancy, and such undercoordinated Ce³⁺ ions due to Ru doping on the surface of a small CeO₂ crystal could result in lattice distortion [55].

3.5 Transmission electron microscopy (TEM)

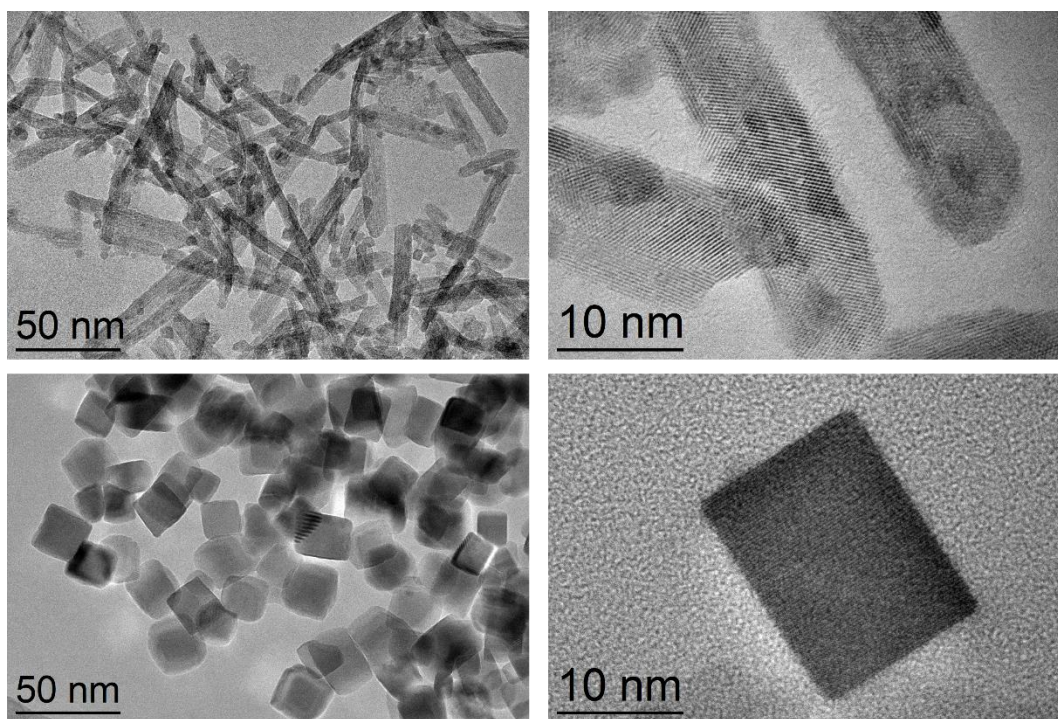


Fig. 7 HRTEM images of 1 wt% Ru/CeO₂ NR-r and 1 wt% Ru/CeO₂ NC-r.

Fig. 7 displays the low and high-magnification TEM images of CeO₂ NR and NC supported RuO_x catalysts. Both rod and cube-shaped CeO₂ supports maintained their initial morphology after Ru loading, calcination, and reduction treatment. The length and diameter of CeO₂ NR for the reduced

sample are in the range of 50 to 80 nm and 5 to 10 nm, respectively. The cube-shaped CeO₂ has an approximate length of 20 to 40 nm. The Ru crystallites are hard to detect due to their smaller size and low doping amount (1 wt%). However, **Fig. 3** indicated the presence of Ru by EDS elemental mapping. The HRTEM images also demonstrate the rough surface of CeO₂ NR, which indicates the presence of lattice distortion, lattice defects, and void, among many other surface defects. The exposed crystal facets of CeO₂ NC are (100) lattice fringes, while CeO₂ NR possesses a mixture of (111), (100), and (011) lattice fringes with the corresponding d-spacing of 3.08-3.16Å, 2.7Å and 1.9Å, respectively, observed from the HRTEM images.

4 Performance test

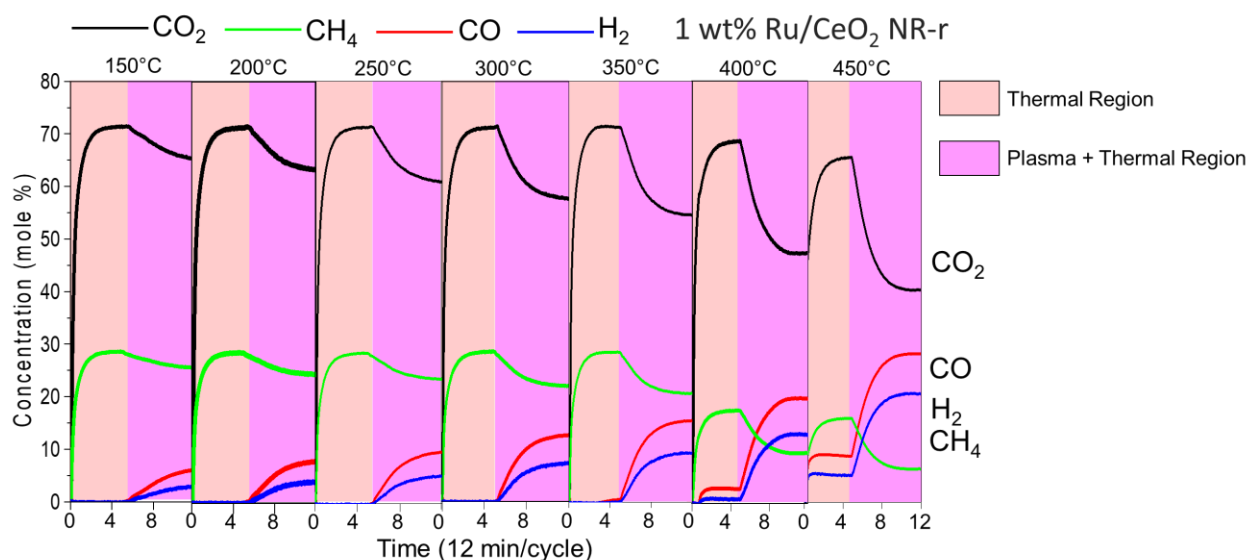


Fig. 8 Measured time-resolved species mole fraction for thermal and thermal + plasma regions from 150 °C to 450 °C, 1 atm pressure (5 min for thermal catalysis only and 7 min for thermal + plasma catalysis) (Catalyst wt.: ~200 mg, Power: 10.2 to 13.6 W, Frequency: 20kHz, Flowrate: CO₂: 250 sccm and CH₄: 100 sccm).

Fig. 8 shows the molar fraction of CO₂, CH₄, CO, and H₂ obtained from Extrel QMS for DRM at seven different temperatures from 150 °C to 450 °C. This "plasma-off-plasma-on" experiment was designed to understand the synergistic effect of plasma and thermal catalysis in DRM. The plasma was introduced for seven minutes, initiating from the 6th minute and stopping at the 12th minute, followed by a 5-minute thermal only DRM reaction. The effect of introducing plasma in a thermal DRM is very clear from **Fig. 8**, where two different colors indicate thermal and plasma + thermal regions. For example, at 150 °C, initially, there were "no detectable" CO and H₂ gases during five minutes of thermal catalysis region. Once the initiation of plasma at the 6th minute, CO (red line) and H₂ (blue line) gases were clearly observed with a sudden decrease in mole concentration of supplied CO₂ (black line) and CH₄ (green line). For the thermal catalysis region at 150 °C, the mole percentage of both CO and H₂ was "zero", which changed to 7% and 3%, respectively, when plasma was introduced. In this project, we utilized both thermopile infrared array sensor and infrared thermometer to measure the surface temperature of the catalysts. It should be noted that the measured surface temperature of the catalysts is reasonably close (10-40 °C) to the reactor temperature as shown in **Fig. S4**. There were "no detectable" CO and H₂ till 350 °C for thermal-driven DRM. Thus, in the temperature range from 150 °C to 350 °C of the plasma + thermal region, the conversion of CH₄ and CO₂ gradually increased, which is due to the introduction of non-thermal plasma. The mole percentage of CO and H₂ increased from 7% to 16% and 3% to 9% from 150 °C to 350 °C in the plasma + thermal region. This indicates that the introduction of plasma plays a crucial role in initiating and promoting low-temperature DRM to produce syngas. For 400 °C and 450 °C, CO and H₂ concentrations were less than 10% for thermal DRM. For example, for the thermal region at 450 °C, CO and H₂ concentration were 9% and 5%. However, for the plasma + thermal region at 450 °C, these concentrations were 28% and 21% for CO and H₂, respectively,

which are significantly higher than those in the thermal-only DRM regions. The CO and H₂ molar concentration vs time at temperature between 150 °C to 450 °C is shown in **Fig. S5**. At low temperatures, it takes time for the reaction to reach equilibrium, whereas at high temperatures, it stabilizes rapidly. In **Fig. S6**, a 10 min plasma-assisted reduction cycle for 1 wt% Ru/CeO₂ NR-r catalyst at 250 °C was shown, which clearly illustrates that there was no noticeable change from MS in molar concentration of CO₂, CH₄, CO, or H₂ after 7 minutes. According to our Quantum Cascade Laser (QCL) absorption system, a very tiny amount of C₂H₆ or ethane was detected during plasma-assisted DRM as shown in **Fig. S7**.

Fig. 9 shows the conversion of DRM reaction with only plasma, plasma-assisted only support, plasma-assisted catalyst, and thermal catalysts at 450 °C, 400 °C, and 350 °C. It is noticeable that plasma-assisted DRM is extraordinarily high compared to thermal-driven DRM. Plasma and catalyst synergism highly enhanced the DRM conversion close to 51% and 37% for CH₄ and CO₂, respectively, at 450 °C. However, DRM conversion with only plasma and plasma-assisted only support was less than 5% for both CH₄ and CO₂.

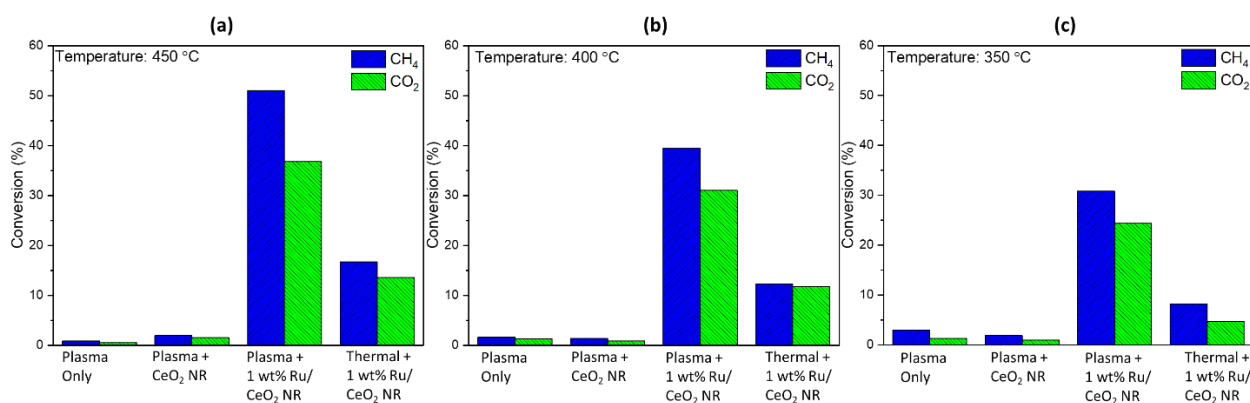


Fig. 9 CH₄ and CO₂ conversion with only plasma, plasma + CeO₂ NR, plasma + 1 wt% Ru/CeO₂ NR and thermal + 1 wt%/CeO₂ NR at (a) 450 °C, (b) 400 °C and (c) 350 °C.

(Catalyst wt.: ~200 mg, Power: 10.2 to 13.6 W, Frequency: 20kHz, Flowrate: CO₂: 250 sccm and CH₄: 100 sccm).

All the CO₂, CH₄, CO, and H₂ species profiles acquired from QMS were time integrated to obtain the total amounts of the products at each temperature which were later used for quantitative calculation of conversion, selectivity, and yield shown in **Figs. 10** and **11**.

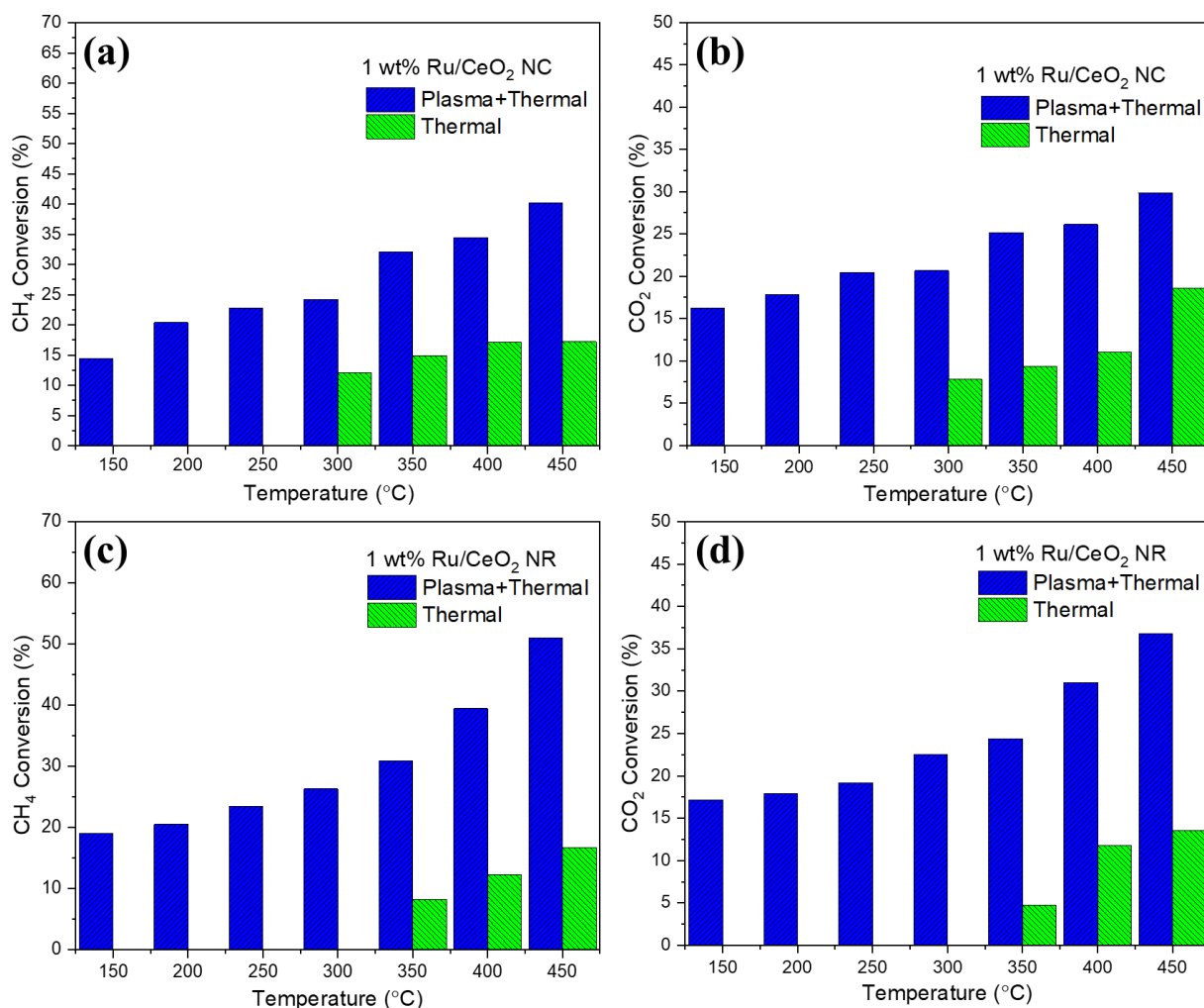


Fig. 10. (a) CH₄ and (b) CO₂ conversion of 1 wt% Ru/CeO₂ NC; (c) CH₄ and (d) CO₂ conversion of 1 wt% Ru/CeO₂ NR from 150 °C to 450 °C under thermal and thermal +

plasma conditions. (Catalyst wt.: ~200 mg, Power: 10.2 to 13.6 W, Frequency: 20kHz, Flowrate: CO₂: 250 sccm and CH₄: 100 sccm).

The conversion of the reactants CH₄ and CO₂ under thermal only and plasma + thermal conditions is presented in **Fig. 10 (a-d)** in the temperature range 150 °C to 450 °C for two catalysts: 1 wt% Ru/CeO₂ NR and 1 wt% Ru/CeO₂ NC. These experimental results were obtained from the reaction conditions where the catalysts were placed in the plasma zone with a constant temperature zone of the furnace. In this case, plasma was in direct contact with the catalyst, and the furnace temperature seriously influenced the plasma zone. It is important to mention that no conversion occurred in thermal DRM till 250 °C for 1 wt% Ru/CeO₂ NC and 300 °C for 1 wt% Ru/CeO₂ NR, which is consistent with the observations in the literature due to the endothermic nature of DRM reaction [56]. Typically for thermal-driven DRM, the conversion of CH₄ and CO₂ was observed in operating temperatures higher than 300 °C [50]. For thermal-driven DRM, CH₄ conversion percentage is typically lower compared to CO₂ conversion, which may be a result of simultaneous reverse water-gas shift (RWGS) reaction ($CO_2 + H_2 = CO + H_2O$) [57]. The conversion trends of CH₄ and CO₂ over 1 wt% Ru/CeO₂ NC and 1 wt% Ru/CeO₂ NR samples are similar, and the conversion percentage of 1 wt% Ru/CeO₂ NC was “even” higher than 1 wt% Ru/CeO₂ NR under thermal driven DRM. For example, at 450 °C, CO₂ conversion was 17% for 1 wt% Ru/CeO₂ NC, which is 3% greater than 1 wt% Ru/CeO₂ NR (14%). For similar work, Zhou et al. [58] reported that the reaction rate of Ru dispersed on CeO₂ NC was higher than that of Ru dispersed on CeO₂ NR. Although kinetic modeling indicates similar turnover frequency (TOF) for CeO₂ NC and CeO₂ NR based on surface-oxygen vacancies ($2.67\sim 2.91 * 10^{-4} s^{-1}$) and activation energies ($72.9\sim 76.4 kJmole^{-1}$), the higher performance of thermal driven DRM over 1 wt% Ru/CeO₂ NC

resides in oxygen vacancy concentration between RuO_x-CeO₂ interface. Compared to thermal-driven DRM, **Fig. 10 (a-d)** shows that reaction conversion for both CH₄ and CO₂ for plasma-assisted DRM is extraordinarily high. It is clear that the trigger temperature of plasma-assisted thermo-catalytic DRM was at least 250 °C lower than that of thermo-catalytic DRM. Under non-thermal plasma condition, the collision frequency between electrons and gas molecules increases dramatically, followed by the generation of highly energetic electrons, and lead to the generation of more active species such as ions, radicals, etc. For instance, the reactant CH₄ can dissociate into CH_x (x=0, 1, 2, 3) and active H atoms, which are later combined with cracked products from CO₂ and form products such as CO and H₂ [59]. The obtained conversion of CH₄ and CO₂ was from a range of ~19% to ~51% and ~17% to ~37%, respectively, for 1 wt% Ru/CeO₂ NR from 150 °C to 450 °C. For 1 wt% Ru/CeO₂ NC, the conversion was ~14% to ~40% for CH₄ and ~16% to ~30% for CO₂. The higher CH₄ conversion than CO₂ conversion may result from CH₄ dissociation reaction and carbon deposition [60]. Because excessive coking could happen due to a lack of balance between carbon atoms from CH₄ dissociation and carbon atom dislodged by active O atoms from CO₂ dissociation. Similarly, Zheng et al. [59] reported higher CH₄ conversion than CO₂ at higher discharge power which complied with our results. They also reported higher CO selectivity than H₂, and their trend was similar to our results shown in **Fig. 11**. For plasma-assisted DRM, it is worth mentioning that 1 wt% Ru/CeO₂ NR was more active than 1 wt% Ru/CeO₂ NC. Therefore, the shape and/or exposed crystal planes of CeO₂ support played a role in DRM. The conversion of CH₄ increased from 40% (1 wt% Ru/CeO₂ NC) to 51% (1 wt% Ru/CeO₂ NR) at 450 °C whereas CO₂ conversion increased from 30% (1 wt% Ru/CeO₂ NC) to 37% (1 wt% Ru/CeO₂ NR) at the same temperature. Because CeO₂ NR is predominantly exposed with (110) and (100) or defected (111) facets which can anchor higher content of Ru⁴⁺ species and provide a greater

amount of Ru-O-Ce solid solution, compared to CeO₂ NC. In addition, Ru clusters on reducible CeO₂ support give rise to partially oxidized Ru, reduced by CeO₂ (Ru^{δ+}-CeO_{2-x}) to provide active chemistry for better conversion selectivity and yield. It is also concluded from the literature that plasma can bring in more basic sites and smaller crystal sizes of catalysts that promote higher reactivity [61]. The catalyst into the plasma zone accelerates the externally applied electric field and creates stronger micro-discharge and surface discharge. A greater number of exciting species can be ruptured from the collisions between highly energetic electrons and reactants molecules which could be adsorbed over the catalysts to achieve the desired products. Based on the carbon balance analysis of 1 wt% Ru/CeO₂ NR-r catalyst shown in **Fig. S8**, it is reflected that approximately 10% deposited carbon was observed from Boudouard or other coking reactions (i.e., CH₄ decomposition). In addition, a very tiny amount of C₂H₆ or ethane was detected via quantum cascade laser absorption spectroscopy (TDLAS) system, as shown in **Fig. S7**. A few possible reasons for this low carbon deposition are: 1) Ru is known for reducing carbon deposition; 2) more CO₂ was supplied than CH₄ during the reaction for enough metastable O ions that can hinder the CH_x recombination and/or can react with the deposited carbon on the catalyst surface; and 3) below 450 °C, CH₄ decomposition is probably preferable, which produces reactive and less stable carbon species. A CH₄ and CO₂ conversion comparison is present in **Fig. S9**, for CeO₂ supports with plasma and under plasma only conditions. With plasma only condition, both CH₄ and CO₂ conversion were very low compared to Ru doped CeO₂ catalysts. The result showed a maximum 3.5% and 5.5% conversion of CH₄ and CO₂, respectively, with plasma-assisted support and bare plasma. Hence, a small amount of Ru incorporation dramatically increases the performance. The experimental data on the DRM performance under thermal catalysis and plasma-assisted catalysis using 1 wt% Ru/SiO₂ catalyst is presented in **Fig. S10**.

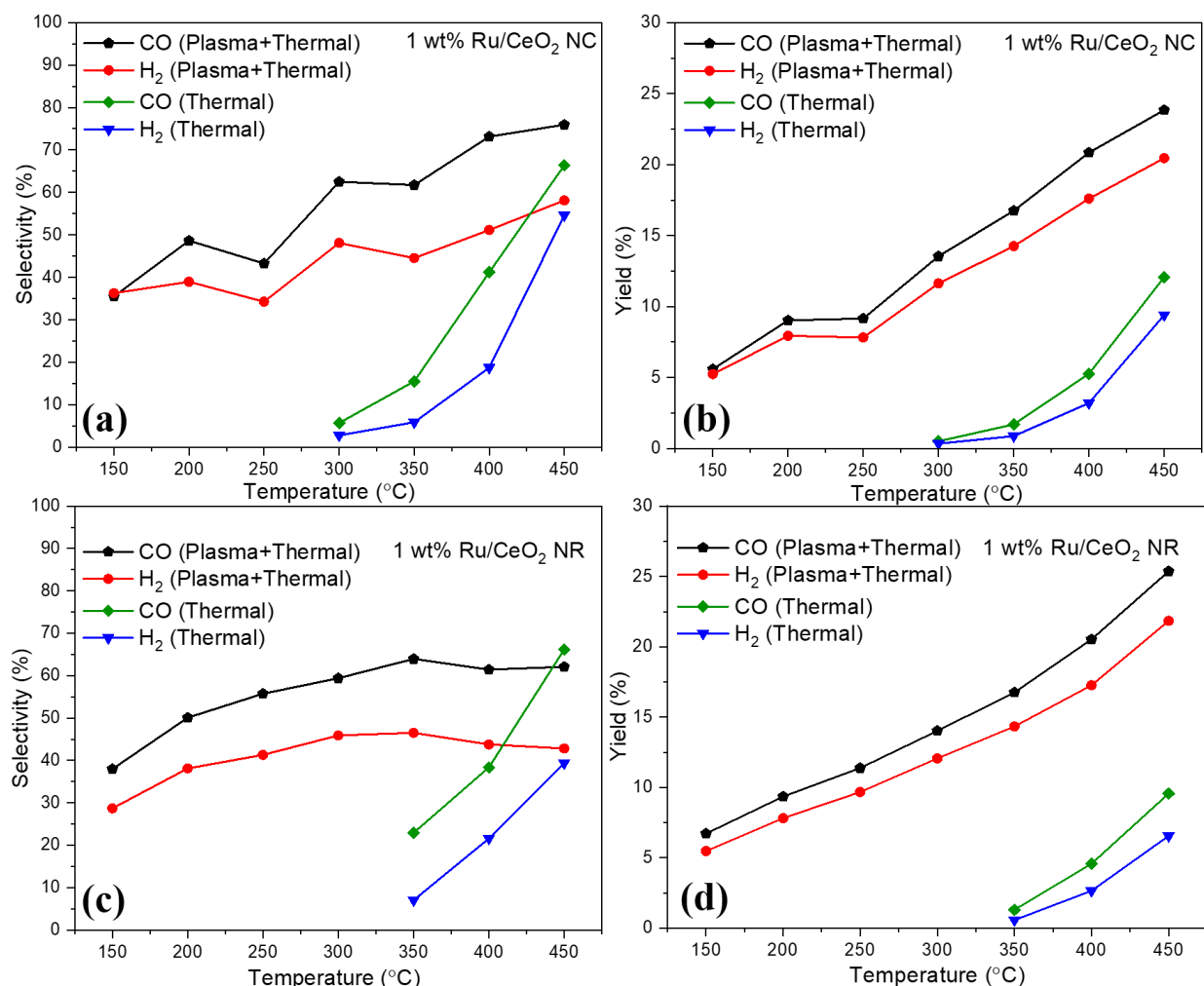


Fig. 11. CO and H₂ (a) selectivity and (b) yield of 1 wt% Ru/CeO₂ NC; (c) selectivity and (d) yield of 1 wt% Ru/CeO₂ NR from 150 °C to 450 °C under thermal and thermal + plasma conditions. (Catalyst wt.: ~200 mg, Power: 10.2 to 13.6 W, Frequency: 20 kHz, Flowrate: CO₂: 250 sccm and CH₄: 100 sccm).

As shown in Fig. 11, yield and selectivity increased with the temperature increase. The maximum CO selectivity and yield were 75% and 25% for 1 wt% Ru/CeO₂ NC, while for H₂, these were 60% and 22% at 450 °C. The selectivity of CO was better than that of H₂ due to the formation of hydrocarbon [62]. In addition, at higher temperatures, the selectivity of H₂ tends to diminish due to

the enhancement of RWGS [63,64]. Moreover, the side products and carbon deposition play a crucial role in the selectivity and yield of desired products [65]. In a catalytic gas-solid reaction, reactants conversion is inversely proportional to desired product selectivity due to the evolution of secondary gas phase reaction [66]. The produced H_2/CO ratio was less than the unity shown in **Fig. 12**, which indicates that CO production was higher than H_2 . This is probably due to the side reactions [67]. RWGS reaction ($CO_2 + H_2 = CO + H_2O$; $\Delta H_{298} = 41 \text{ kJ/mol}$) is another possible reason for the low H_2/CO ratio, which is a common phenomenon in catalytic DRM [62]. This side reaction can consume the produced H_2 , reduce the H_2 yield, and increase CO production. However, the H_2/CO ratio tends to increase gradually with temperature, which indicates that at elevated temperatures, the CeO_2 supported RuO_x catalysts enhanced both DRM and Boudouard reactions given below [68].

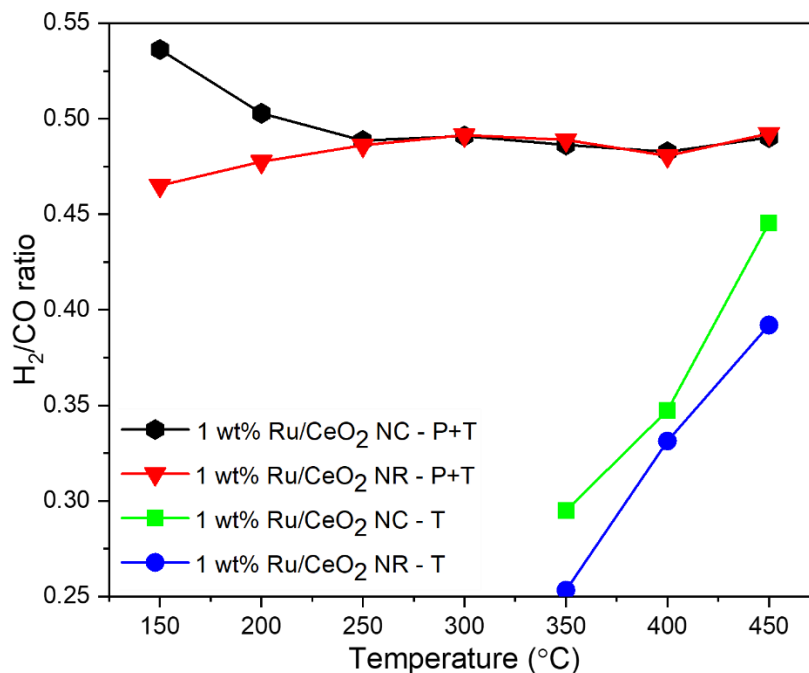
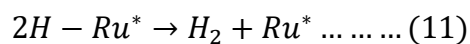
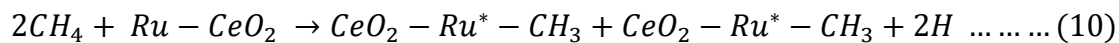


Fig. 12. H₂/ CO ratio of 1 wt% Ru/CeO₂ NC and 1 wt% Ru/CeO₂ NR catalysts from 150 °C to 450 °C under thermal and thermal + plasma conditions. (Catalyst wt.: ~200 mg, Power: 10.2 to 13.6 W, Frequency: 20kHz, Flowrate: CO₂: 250 sccm and CH₄: 100 sccm).

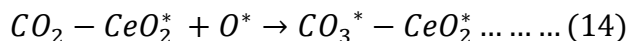
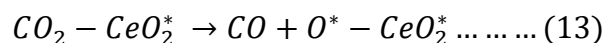
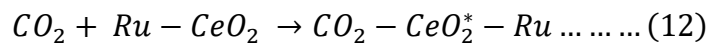
The addition of RuO_x on CeO₂ supports causes a significant increase in oxygen vacancy concentration due to the interaction of RuO_x and CeO₂ at their interface. For 1 wt% Ru/CeO₂ NR- r the relative oxygen content was 49.5%, calculated from XPS characterization. Sakpal et al. [69] reported that 1 wt% Ru/CeO₂ NC promotes a higher concentration of OH and/or carbonate groups and lowers the concentration of oxygen vacancy compared to 1 wt% Ru/CeO₂ NR for CO₂ methanation. On the other side, exposed (110) and (100) or defected (111) facets by CeO₂ NR have lower oxygen vacancy formation energy and high oxygen vacancy concentration. The interaction of RuO_x species with these CeO₂ facets enhances the activation of CO₂ during the reaction and promotes high catalytic activity in the methane dry reforming reaction.

4.1 Reaction Mechanism

For catalytic DRM reaction under thermal-only conditions: it is generally assumed that, for supported Ru catalysts, catalytic DRM is initiated by CH₄ decomposition on active metal Ru sites. At the same time, CO₂ adsorption/dissociation occurs on the support surface [70]. The step-wise CH₄ decomposition leads to CH₄ → CH₃ → CH₂ → CH and C with H₂ production with the following possible surface reactions.



On the other side, CO₂ adsorption on support leads to either directly dissociating CO₂ to CO and adsorbing oxygen or forming carbonate precursor with further possible reaction routes given in **Eq. 14** below.



It should be noted that the produced carbonate precursor is considered a highly reactive intermediate that can promote both CO and H₂ production as well as hydrocarbon formation by interacting with CH_x and spillover H from CH₄ dissociation from active metal site to support.

For plasma-assisted DRM reaction, a possible mechanism can be explained as follows. Plasma and/or high energetic electrons first initiate the activation and dissociation of CO₂ and CH₄, which is followed by the adsorption of intermediate species of CH_x, C, O, H, CO₃^{*} on the metal and support. This adsorption later leads to numerous reaction routes.

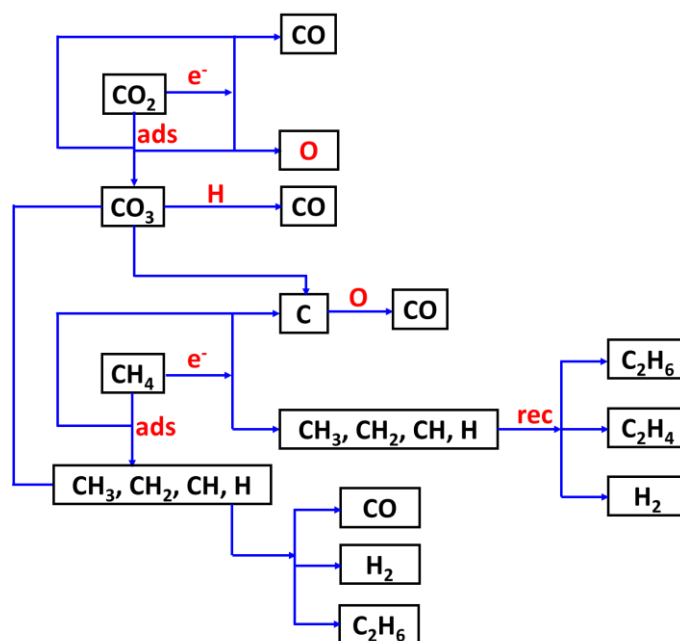
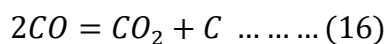
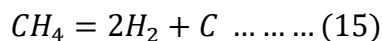


Fig. 13. Possible reaction pathways for the formation of CO, H₂, C₂H₆, and carbon deposition in the direct reforming of CH₄ and CO₂ with DBD.

The dry reforming of methane technique commonly faces the risk of coking or carbon formation at high temperatures mainly either by the methane decomposition (**Eq. 15**: methane cracking) or the Boudouard reaction (**Eq. 16**). This is because these two reactions are favored at lower temperatures (i.e., 300 °C to 500 °C), which is similar to the furnace (gas) temperature range of 150 °C to 450 °C during the plasma-assisted reactions.



Carbon species from the methane decomposition reaction are more reactive than from the Boudouard reaction [71]. According to our experimental temperature range, methane

decomposition is highly favored, while Boudouard or other coking reactions are unlikely to occur. The provided carbon balance profile (**Fig. S8**) and EDX spectrum (**Fig. S11**) of 1 wt% Ru/CeO₂ NR-r catalyst showed approximately 90% that reflects a minimal amount of deposited carbon from Boudouard or other coking reactions and a small amount of C₂H₆ (**Eq. 21**) from methane decomposition (**Fig. S7**). The production of C-2 species (such as C₂H₂, C₂H₄, C₂H₆) is higher at 150 °C, decreases with increasing reaction temperature, and becomes close to zero when the temperature exceeds 300 °C. The STEM and HRTEM images of the spent 1 wt% Ru/CeO₂ NR catalyst are shown in **Fig. S12**. At lower temperatures, the catalyst and plasma synergy produces more CH₃ and CH₂ radicals instead of deposited carbon, and these radicals move the reaction directly to the production of C-2 species. Although methane decomposition promotes amorphous carbon deposition on active RuO_x sites, this was efficiently oxidized by the redox properties of CeO₂ support (Ce³⁺/Ce⁴⁺). The strong metal support interaction of Ru and CeO₂ support formed a solid solution of partially oxidized Ru on reduced CeO₂ support with the chemical formula Ru^{δ+}-CeO_{2-x}. Thus, higher oxygen transfer between Ru and ceria allowed surface carbon gasification and produced CO.

5 Conclusion

In summary, three different oxides (CeO₂ NR, CeO₂ NC, and SiO₂) supported 1 wt% Ru catalysts were prepared to study plasma-assisted DRM under non-equilibrium conditions. The reduced 1 wt% Ru/CeO₂ NR showed higher surface basicity and oxygen vacancy concentration and superior low-temperature activity for DRM compared to the 1 wt% Ru/CeO₂ NC and 1 wt% Ru/SiO₂ catalysts. The introduction of non-thermal plasma in a DBD reactor promoted low-temperature

DRM conversion over 1 wt% Ru/CeO₂ NR and 1 wt% Ru/CeO₂ NC catalysts compared to the catalyst activity under thermal catalysis only conditions. Compared to 1 wt% Ru/CeO₂ NC-r, 1 wt% Ru/CeO₂ NR-r catalyst presented 11% higher CH₄ conversion and 7% CO₂ conversion at 450 °C. The enhanced DRM activity with CeO₂ NR as catalyst support is attributed to the highly exposed surface faces and a greater number of surface defects (i.e., Ce³⁺, oxygen vacancy, and rough surface).

Acknowledgment: This project is supported by the grants from the National Science Foundation (CBET 1856729 and IIP 2044733). We are thankful of Prof. Martin G. Bakker for the help of the measurements of the N₂ physisorption isotherms and pore size distribution. This project also receives partial financial support from Alabama Transportation Institute and Alabama Water Institute. The use of electron microscopy facilities at the Alabama Analytical Research Center (AARC) at The University of Alabama is gratefully acknowledged.

References

- [1] P. Friedlingstein, R.A. Houghton, G. Marland, J. Hackler, T.A. Boden, T.J. Conway, J.G. Canadell, M.R. Raupach, P. Ciais, C. Le Quéré, Update on CO₂ emissions, *Nat Geosci.* 3 (2010) 811–812.
- [2] Y. Zheng, W. Zhang, Y. Li, J. Chen, B. Yu, J. Wang, L. Zhang, J. Zhang, Energy related CO₂ conversion and utilization: Advanced materials/nanomaterials, reaction mechanisms and technologies, *Nano Energy.* 40 (2017) 512–539.
- [3] P. Mehta, P. Barboun, D.B. Go, J.C. Hicks, W.F. Schneider, Catalysis Enabled by Plasma Activation of Strong Chemical Bonds: A Review, *ACS Energy Lett.* 4 (2019) 1115–1133.
- [4] G.A. Olah, A. Goepfert, M. Czaun, T. Mathew, R.B. May, G.K.S. Prakash, Single step bi-reforming and oxidative bi-reforming of methane (natural gas) with steam and carbon dioxide to metgas (CO-2H₂) for methanol synthesis: self-sufficient effective and exclusive oxygenation of methane to methanol with oxygen, *J Am Chem Soc.* 137 (2015) 8720–8729.

- [5] A. Galadima, O. Muraza, Catalytic thermal conversion of CO₂ into fuels: Perspective and challenges, *Renewable and Sustainable Energy Reviews*. 115 (2019) 109333.
- [6] D.R. Kauffman, J. Thakkar, R. Siva, C. Matranga, P.R. Ohodnicki, C. Zeng, R. Jin, Efficient electrochemical CO₂ conversion powered by renewable energy, *ACS Appl Mater Interfaces*. 7 (2015) 15626–15632.
- [7] D. Yap, J.-M. Tatibouët, C. Batiot-Dupeyrat, Catalyst assisted by non-thermal plasma in dry reforming of methane at low temperature, *Catal Today*. 299 (2018) 263–271.
- [8] X. Chen, Z. Sheng, S. Murata, S. Zen, H.-H. Kim, T. Nozaki, CH₄ dry reforming in fluidized-bed plasma reactor enabling enhanced plasma-catalyst coupling, *Journal of CO₂ Utilization*. 54 (2021) 101771.
- [9] J.A. Andersen, J.M. Christensen, M. Østberg, A. Bogaerts, A.D. Jensen, Plasma-Catalytic Dry Reforming of Methane: Screening of Catalytic Materials in a Coaxial Packed-Bed DBD Reactor, *Chemical Engineering Journal*. (2020) 125519.
- [10] M.H. Pham, V. Goujard, J.M. Tatibouët, C. Batiot-Dupeyrat, Activation of methane and carbon dioxide in a dielectric-barrier discharge-plasma reactor to produce hydrocarbons—Influence of La₂O₃/γ-Al₂O₃ catalyst, *Catal Today*. 171 (2011) 67–71.
- [11] X. Zheng, S. Tan, L. Dong, S. Li, H. Chen, LaNiO₃@SiO₂ core-shell nano-particles for the dry reforming of CH₄ in the dielectric barrier discharge plasma, *Int J Hydrogen Energy*. 39 (2014) 11360–11367.
- [12] H.J. Gallon, X. Tu, J.C. Whitehead, Effects of reactor packing materials on H₂ production by CO₂ reforming of CH₄ in a dielectric barrier discharge, *Plasma Processes and Polymers*. 9 (2012) 90–97.
- [13] A.H. Khoja, M. Tahir, N.A.S. Amin, Cold plasma dielectric barrier discharge reactor for dry reforming of methane over Ni/γ-Al₂O₃-MgO nanocomposite, *Fuel Processing Technology*. 178 (2018) 166–179.
- [14] M.C.J. Bradford, M.A. Vannice, CO₂ Reforming of CH₄ over Supported Ru Catalysts, *J Catal*. 183 (1999) 69–75.
- [15] D. Sutton, S.M. Parle, J.R.H. Ross, The CO₂ reforming of the hydrocarbons present in a model gas stream over selected catalysts, *Fuel Processing Technology*. 75 (2002) 45–53.
- [16] D. Qin, J. Lapszewicz, Study of mixed steam and CO₂ reforming of CH₄ to syngas on MgO-supported metals, *Catal Today*. 21 (1994) 551–560.
- [17] J. Wei, E. Iglesia, Reaction pathways and site requirements for the activation and chemical conversion of methane on Ru-based catalysts, *J Phys Chem B*. 108 (2004) 7253–7262.
- [18] A. Aitbekova, L. Wu, C.J. Wrasman, A. Boubnov, A.S. Hoffman, E.D. Goodman, S.R. Bare, M. Cargnello, Low-temperature restructuring of CeO₂-supported Ru nanoparticles determines selectivity in CO₂ catalytic reduction, *J Am Chem Soc*. 140 (2018) 13736–13745.
- [19] C.H. Bartholomew, Mechanisms of catalyst deactivation, *Appl Catal A Gen*. 212 (2001) 17–60.

- [20] P. Ferreira-Aparicio, I. Rodriguez-Ramos, J.A. Anderson, A. Guerrero-Ruiz, Mechanistic aspects of the dry reforming of methane over ruthenium catalysts, *Appl Catal A Gen.* 202 (2000) 183–196.
- [21] N.J. Lawrence, J.R. Brewer, L. Wang, T.-S. Wu, J. Wells-Kingsbury, M.M. Ihrig, G. Wang, Y.-L. Soo, W.-N. Mei, C.L. Cheung, Defect engineering in cubic cerium oxide nanostructures for catalytic oxidation, *Nano Lett.* 11 (2011) 2666–2671.
- [22] J.A. Rodríguez, J. Hrbek, Inverse oxide/metal catalysts: A versatile approach for activity tests and mechanistic studies, *Surf Sci.* 604 (2010) 241–244.
- [23] P.X. Huang, F. Wu, B.L. Zhu, X.P. Gao, H.Y. Zhu, T.Y. Yan, W.P. Huang, S.H. Wu, D.Y. Song, CeO₂ Nanorods and Gold Nanocrystals Supported on CeO₂ Nanorods as Catalyst, *J Phys Chem B.* 109 (2005) 19169–19174.
- [24] H.-X. Mai, L.-D. Sun, Y.-W. Zhang, R. Si, W. Feng, H.-P. Zhang, H.-C. Liu, C.-H. Yan, Shape-Selective Synthesis and Oxygen Storage Behavior of Ceria Nanopolyhedra, Nanorods, and Nanocubes, *J Phys Chem B.* 109 (2005) 24380–24385.
- [25] C. Ho, J.C. Yu, T. Kwong, A.C. Mak, S. Lai, Morphology-Controllable Synthesis of Mesoporous CeO₂ Nano- and Microstructures, *Chemistry of Materials.* 17 (2005) 4514–4522.
- [26] Y. Wang, Z. Liu, R. Wang, NaBH₄ Surface Modification on CeO₂ Nanorods Supported Transition-Metal Catalysts for Low Temperature CO Oxidation, *ChemCatChem.* 12 (2020) 4304–4316.
- [27] Z. Liu, Y. Lu, M.P. Confer, H. Cui, J. Li, Y. Li, Y. Wang, S.C. Street, E.K. Wujcik, R. Wang, Thermally Stable RuO_x–CeO₂ Nanofiber Catalysts for Low-Temperature CO Oxidation, *ACS Appl Nano Mater.* 3 (2020) 8403–8413.
- [28] S. Agarwal, L. Lefferts, B.L. Mojet, D.A.J.M. Ligthart, E.J.M. Hensen, D.R.G. Mitchell, W.J. Erasmus, B.G. Anderson, E.J. Olivier, J.H. Neethling, A.K. Datye, Exposed Surfaces on Shape-Controlled Ceria Nanoparticles Revealed through AC-TEM and Water–Gas Shift Reactivity, *ChemSusChem.* 6 (2013) 1898–1906.
- [29] J. Zhao, Y. He, F. Wang, W. Zheng, C. Huo, X. Liu, H. Jiao, Y. Yang, Y. Li, X. Wen, Suppressing Metal Leaching in a Supported Co/SiO₂ Catalyst with Effective Protectants in the Hydroformylation Reaction, *ACS Catal.* 10 (2019) 914–920.
- [30] R. Wang, R. Dangerfield, Seed-mediated synthesis of shape-controlled CeO₂ nanocrystals, *RSC Adv.* 4 (2014) 3615–3620.
- [31] S.A. Mock, E.T. Zell, S.T. Hossain, R. Wang, Effect of Reduction Treatment on CO Oxidation with CeO₂ Nanorod-Supported CuO_x Catalysts, *ChemCatChem.* 10 (2018) 311–319.
- [32] J. Li, Z. Liu, R. Wang, Support structure and reduction treatment effects on CO oxidation of SiO₂ nanospheres and CeO₂ nanorods supported ruthenium catalysts, *J Colloid Interface Sci.* 531 (2018) 204–215.
- [33] M.R. Ahasan, Y. Wang, R. Wang, In situ DRIFTS and CO-TPD studies of CeO₂ and SiO₂ supported CuO_x catalysts for CO oxidation, *Molecular Catalysis.* 518 (2022) 112085.

- [34] Z. Wei, R. Wang, Chemically etched CeO_{2-x} nanorods with abundant surface defects as effective cathode additive for trapping lithium polysulfides in Li-S batteries, *J Colloid Interface Sci.* 615 (2022) 527–542.
- [35] Z. Zhao, Redox kinetics study for chemical-looping combustion, water and CO₂ splitting using nickel and cerium-based oxygen carrier, (2016).
- [36] Z. Zhao, M. Uddi, N. Tsvetkov, B. Yildiz, A.F. Ghoniem, Redox kinetics study of fuel reduced ceria for chemical-looping water splitting, *The Journal of Physical Chemistry C.* 120 (2016) 16271–16289.
- [37] N.A.S. Amin, Co-generation of synthesis gas and C₂₊ hydrocarbons from methane and carbon dioxide in a hybrid catalytic-plasma reactor: A review, *Fuel.* 85 (2006) 577–592.
- [38] Y.P. Raizer, J.E. Allen, *Gas discharge physics*, Springer, 1991.
- [39] T. Yabe, K. Mitarai, K. Oshima, S. Ogo, Y. Sekine, Low-temperature dry reforming of methane to produce syngas in an electric field over La-doped Ni/ZrO₂ catalysts, *Fuel Processing Technology.* 158 (2017) 96–103.
- [40] T. Nozaki, K. Okazaki, Non-thermal plasma catalysis of methane: Principles, energy efficiency, and applications, *Catal Today.* 211 (2013) 29–38.
- [41] M. Farahmandjou, M. Zarinkamar, T.P. Firoozabadi, Synthesis of Cerium Oxide (CeO₂) nanoparticles using simple CO-precipitation method, *Revista Mexicana de Física.* 62 (2016) 496–499.
- [42] J. Li, Z. Liu, D.A. Cullen, W. Hu, J. Huang, L. Yao, Z. Peng, P. Liao, R. Wang, Distribution and Valence State of Ru Species on CeO₂ Supports: Support Shape Effect and Its Influence on CO Oxidation, *ACS Catal.* 9 (2019) 11088–11103.
- [43] F. Wang, C. Li, X. Zhang, M. Wei, D.G. Evans, X. Duan, Catalytic behavior of supported Ru nanoparticles on the {1 0 0}, {1 1 0}, and {1 1 1} facet of CeO₂, *J Catal.* 329 (2015) 177–186.
- [44] C. Fernández, C. Pezzotta, G. Raj, E.M. Gaigneaux, P. Ruiz, Understanding the growth of RuO₂ colloidal nanoparticles over a solid support: An atomic force microscopy study, *Catal Today.* 259 (2016) 183–191.
- [45] Y. Wang, R. Wang, Effects of chemical etching and reduction activation of CeO₂ nanorods supported ruthenium catalysts on CO oxidation., *J Colloid Interface Sci.* 613 (2022) 836–846.
- [46] T. Niu, C.X. Wang, L.H. Zhang, Y. Liu, Potassium promoted Ru/meso-macroporous SiO₂ catalyst for the preferential oxidation of CO in H₂-rich gases, *Int J Hydrogen Energy.* 38 (2013) 7801–7810.
- [47] C.A. Teles, R.C. Rabelo-Neto, J.R. de Lima, L. V Mattos, D.E. Resasco, F.B. Noronha, The effect of metal type on hydrodeoxygenation of phenol over silica supported catalysts, *Catal Letters.* 146 (2016) 1848–1857.

- [48] M.A.A. Aziz, A.A. Jalil, S. Wongsakulphasatch, D.-V.N. Vo, Understanding the role of surface basic sites of catalysts in CO₂ activation in dry reforming of methane: a short review, *Catal Sci Technol*. 10 (2020) 35–45.
- [49] W. Li, G. Zhang, X. Jiang, Y. Liu, J. Zhu, F. Ding, Z. Liu, X. Guo, C. Song, CO₂ hydrogenation on unpromoted and M-promoted Co/TiO₂ catalysts (M= Zr, K, Cs): effects of crystal phase of supports and metal–support interaction on tuning product distribution, *ACS Catal*. 9 (2019) 2739–2751.
- [50] A. Arman, F.Y. Hagos, A.A. Abdullah, R. Mamat, A.R.A. Aziz, C.K. Cheng, Syngas production through steam and CO₂ reforming of methane over Ni-based catalyst-A Review, in: *IOP Conf Ser Mater Sci Eng*, IOP Publishing, 2020: p. 42032.
- [51] I. Luisetto, S. Tuti, C. Romano, M. Boaro, E. Di Bartolomeo, J.K. Kesavan, S.S. Kumar, K. Selvakumar, Dry reforming of methane over Ni supported on doped CeO₂: New insight on the role of dopants for CO₂ activation, *Journal of CO₂ Utilization*. 30 (2019) 63–78.
- [52] J. Ilsemann, M.M. Murshed, T.M. Gesing, J. Kopyscinski, M. Bäumer, On the support dependency of the CO₂ methanation–decoupling size and support effects, *Catal Sci Technol*. (2021).
- [53] X. Li, D. Li, H. Tian, L. Zeng, Z.-J. Zhao, J. Gong, Dry reforming of methane over Ni/La₂O₃ nanorod catalysts with stabilized Ni nanoparticles, *Appl Catal B*. 202 (2017) 683–694.
- [54] Z. Ma, S. Zhao, X. Pei, X. Xiong, B. Hu, New insights into the support morphology-dependent ammonia synthesis activity of Ru/CeO₂ catalysts, *Catal Sci Technol*. 7 (2017) 191–199.
- [55] H. Huang, Q. Dai, X. Wang, Morphology effect of Ru/CeO₂ catalysts for the catalytic combustion of chlorobenzene, *Appl Catal B*. 158 (2014) 96–105.
- [56] J. Horlyck, S. Lewis, R. Amal, J. Scott, The impact of La doping on dry reforming Ni-based catalysts loaded on FSP-alumina, *Top Catal*. 61 (2018) 1842–1855.
- [57] L. He, Y. Ren, Y. Fu, B. Yue, S.C.E. Tsang, H. He, Morphology-dependent catalytic activity of Ru/CeO₂ in dry reforming of methane, *Molecules*. 24 (2019) 526.
- [58] Y. Zhou, Y. Li, W. Shen, Shape engineering of oxide nanoparticles for heterogeneous catalysis, *Chemistry–An Asian Journal*. 11 (2016) 1470–1488.
- [59] X. Zheng, S. Tan, L. Dong, S. Li, H. Chen, Plasma-assisted catalytic dry reforming of methane: Highly catalytic performance of nickel ferrite nanoparticles embedded in silica, *J Power Sources*. 274 (2015) 286–294.
- [60] S. Hamzehlouia, S.A. Jaffer, J. Chaouki, Microwave Heating-Assisted Catalytic Dry Reforming of Methane to Syngas, *Sci Rep*. 8 (2018) 8940.
- [61] Y. Ge, T. He, D. Han, G. Li, R. Zhao, J. Wu, Plasma-assisted CO₂ methanation: effects on the low-temperature activity of an Ni–Ce catalyst and reaction performance, *R Soc Open Sci*. 6 (2019) 190750.
- [62] D. Ray, P.M.K. Reddy, Ch. Subrahmanyam, Ni-Mn/γ-Al₂O₃ assisted plasma dry reforming of methane, *Catal Today*. 309 (2018) 212–218..

- [63] I. Istadi, N.A. Saidina Amin, Co-generation of C₂ hydrocarbons and synthesis gases from methane and carbon dioxide: a thermodynamic analysis, *Journal of Natural Gas Chemistry*. 14 (2005) 140–150.
- [64] H. Tsai, C. Wang, Thermodynamic equilibrium prediction for natural gas dry reforming in thermal plasma reformer, *Journal of the Chinese Institute of Engineers*. 31 (2008) 891–896.
- [65] F. Barrai, T. Jackson, N. Whitmore, M.J. Castaldi, The role of carbon deposition on precious metal catalyst activity during dry reforming of biogas, *Catal Today*. 129 (2007) 391–396.
- [66] M. Usman, W.M.A.W. Daud, H.F. Abbas, Dry reforming of methane: Influence of process parameters—A review, *Renewable and Sustainable Energy Reviews*. 45 (2015) 710–744.
- [67] D. Zambrano, J. Soler, J. Herguido, M. Menéndez, Kinetic study of dry reforming of methane over Ni–Ce/Al₂O₃ catalyst with deactivation, *Top Catal*. 62 (2019) 456–466.
- [68] J.M. Saad, P.T. Williams, Manipulating the H₂/CO ratio from dry reforming of simulated mixed waste plastics by the addition of steam, *Fuel Processing Technology*. 156 (2017) 331–338.
- [69] T. Sakpal, L. Lefferts, Structure-dependent activity of CeO₂ supported Ru catalysts for CO₂ methanation, *J Catal*. 367 (2018) 171–180.
- [70] M. Li, Z. Sun, Y.H. Hu, Catalysts for CO₂ reforming of CH₄: a review, *J Mater Chem A Mater*. 9 (2021) 12495–12520.
- [71] A.S.A.S. Omran, DFT Study of Copper-Nickel (111) Catalyst for Methane Dry Reforming, (2019).